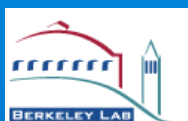




EUV mask blank
inspection at the
ALS



ACTINIC MASK INSPECTION AT THE ALS

INITIAL DESIGN REVIEW

VNL EUV Mask Blank Technology Transfer Program

Anton Barty, Henry Chapman, Don Sweeney,
Rick Levesque and Jay Ayers

*Lawrence Livermore National Laboratory
L-395, PO Box 808, Livermore, CA 94550*

Jeff Bokor, Eric Gullikson, Seongtae Jong, Yanwei Liu,
Moonsuk Yi, Greg Denbeaux, Ken Goldberg, Patrick Naulleau,
Paul Denham, Seno Rekawa, Phil Baston,
Ron Tackaberry, and Paul Barale

*Lawrence Berkeley National Laboratory
1 Cyclotron Road, Berkeley, CA, 94720*

3 April 2003

Submitted to:

Phil Seidel
International SEMATECH
2706 Montopolis Drive
Austin, TX, 78741

DISCLAIMER

This document was prepared as an account of work sponsored by an agency of the United States Government. Neither the United States Government nor the University of California nor any of their employees, makes any warranty, express or implied, or assumes any legal liability or responsibility for the accuracy, completeness, or usefulness of any information, apparatus, product, or process disclosed, or represents that its use would not infringe privately owned rights. Reference herein to any specific commercial product, process, or service by trade name, trademark, manufacturer, or otherwise, does not necessarily constitute or imply its endorsement, recommendation, or favoring by the United States Government or the University of California. The views and opinions of authors expressed herein do not necessarily state or reflect those of the United States Government or the University of California, and shall not be used for advertising or product endorsement purposes.

This is a preprint of a paper intended for publication in a journal or proceedings. Since changes may be made before publication, this preprint is made available with the understanding that it will not be cited or reproduced without the permission of the author.

This work was performed under the auspices of the U.S. Department of Energy by the University of California, Lawrence Livermore National Laboratory under contract number W-7405-ENG-48.

This report has been reproduced directly from the best available copy.

Available electronically at <http://www.doc.gov/bridge>

Available for a processing fee to U.S. Department of Energy
And its contractors in paper from
U.S. Department of Energy
Office of Scientific and Technical Information
P.O. Box 62
Oak Ridge, TN 37831-0062
Telephone: (865) 576-8401
Facsimile: (865) 576-5728
E-mail: reports@adonis.osti.gov

Available for the sale to the public from
U.S. Department of Commerce
National Technical Information Service
5285 Port Royal Road
Springfield, VA 22161
Telephone: (800) 553-6847
Facsimile: (703) 605-6900
E-mail: orders@ntis.fedworld.gov
Online ordering: <http://www.ntis.gov/ordering.htm>

OR

Lawrence Livermore National Laboratory
Technical Information Department's Digital Library
<http://www.llnl.gov/tid/Library.html>

CONTENTS

1	SCOPE AND CONTEXT OF THE REPORT	3
2	BACKGROUND	3
2.1	BRIGHT-FIELD AND DARK-FIELD IMAGING MODES	4
2.2	SCATTERING FROM A CRITICAL DEFECT	5
2.3	KEY OPTICAL SYSTEM PARAMETERS	6
2.4	SELECTION OF BEAMLINE	8
3	OVERVIEW OF CANDIDATE SYSTEMS.....	8
3.1	EXISTING SYSTEM USING GRAZING INCIDENCE KIRKPATRICK-BAEZ OPTICS.....	8
3.2	SCANNING SYSTEM WITH 10X OPTICS	9
3.3	SCANNING SYSTEM WITH ZONE PLATE OPTICS	11
3.4	ZONE PLATE IMAGING SYSTEM	11
3.5	COMPARATIVE ANALYSIS OF THROUGHPUT RATES	13
4	PRELIMINARY SYSTEM DESIGN.....	20
4.1	BASELINE SYSTEM DESCRIPTION	20
4.2	CONCEPTUAL DESIGN FOR HIGH-SPEED SCANNING	24
4.3	KEY SUBSYSTEMS	27
4.4	CONCEPTUAL DESIGN FOR HIGH-RESOLUTION IMAGING	32
4.5	PRELIMINARY SUBSYSTEM SPECIFICATIONS	35
5	USEFUL ADDITIONAL INFORMATION.....	38
5.1	PHOTON FLUX MEASUREMENT AT BL 11.3.2.....	38
5.2	SIDE ELEVATION OF CURRENT BEAMLINE	40
5.3	FLOOR PLAN OF BEAMLINE	41

This work was performed under the auspices of the U.S. Department of Energy by University of California Lawrence Livermore National Laboratory under contract No. W-7405-Eng-48 and University of California Lawrence Berkeley National Laboratory. This project is supported by International SEMATECH under Project Lith 343.
UCRL-CR-152460

1 Scope and context of the report

This report is the first milestone report for the actinic mask blank inspection project conducted at the VNL, which forms sub-section 3 of the Q1 2003 mask blank technology transfer program at the VNL. Specifically this report addresses deliverable 3.1.1 – design review and preliminary tool design.

The goal of this project is to design an actinic mask inspection tool capable of operating in two modes: high-speed scanning for the detection of multilayer defects (inspection mode), and a high-resolution aerial image mode in which the image emulates the imaging illumination conditions of a stepper system (aerial image or AIM mode). The purpose and objective of these two modes is as follows:

Defect inspection mode

This imaging mode is designed to scan large areas of the mask for defects EUV multilayer coatings. The goal is to detect the presence of multilayer defects on a mask blank and to store the co-ordinates for subsequent review in AIM mode, thus it is not essential that the illumination and imaging conditions match that of a production stepper. Potential uses for this imaging mode include:

- Correlating the results obtained using actinic inspection with results obtained using other non-EUV defect inspection systems to verify that the non-EUV scanning systems are detecting all critical defects;
- Gaining sufficient information to associate defects with particular processes, such as various stages of the multilayer deposition or different modes of operation of the deposition tool; and
- Assessing the density and EUV impact of surface and multilayer anomalies

Because of the low defect density achieved using current multilayer coating technology it is necessary to be able to efficiently scan large areas of the mask in order to obtain sufficient statistics for use in cross-correlation experiments. Speed of operation as well as sensitivity is therefore key to operation in defect inspection mode.

Aerial Image Microscope (AIM) mode

In AIM mode the tool is configured so that the collected data emulates the aerial image of a stepper system, thereby enabling rapid evaluation of mask defects and patterning without the need for a resist exposure step. The main uses of the microscope in this mode would be:

- Review of multilayer and pattern defects to determine their printability
- Defect review following a repair process to assess the success of the operation
- Investigation of the effects of illumination and NA on the printed image
- Process window analysis of defects and other mask features
- Characterising defects on both patterned and unpatterned masks (i.e. blanks)

An essential characteristic of operation in this mode is that the illumination and imaging conditions through focus should emulate as accurately as possible that of a production stepper system. This mode is designed for local review of defects over a small sub-field of the mask; therefore it is not necessary to have the same high-speed throughput required for defect inspection mode.

We first describe some technical background relating to EUV masks and defect scanning, with the aim of defining the context of the tool and experiments to be performed. We then present an overview of several candidate optical system configurations for achieve the above objectives, and analyse the ability of each system to achieve the stated project goals. Of key importance is throughput and sensitivity in inspection mode, whilst in AIM mode key points are spatial resolution and the ability to perform stepper emulation imaging. We then down-select the best candidate from this set of solutions to one system, which is then investigated in further detail with a view to producing a preliminary tool design and estimates of overall system performance.

2 Background

A defect is any area on the mask that causes unwanted variations in EUV dose in the aerial image obtained in a printing tool. In reflective EUV masks defects can occur in both the reflective mask substrate and the patterned absorber layer. Defects in the patterned absorber layer consist of regions where metal, typically chrome, is unintentionally added or removed from the pattern leading to errors in the reflected field. There currently exists a mature technology for inspecting and repairing defects in the mask pattern. However, a problem unique to EUVL is the existence of defects in the reflective multilayer coating applied to mask blanks prior to patterning. These defects can also perturb the reflected field, causing unwanted variations in the aerial image contrast, and manifesting themselves as defects in the printed image.

A typical EUV multilayer coating consists of 40-80 bilayers of molybdenum and amorphous silicon with each bilayer consisting of approximately 3nm Mo and 4nm Si. The reflectivity of the multilayer is a resonant property of the alternating layer structure and is at an optimum when all the layers interfere constructively; because reflection takes place throughout the bulk of the multilayer any deformation or disruption of the layer structure can manifest itself as a defect. Ideally the goal is to produce defect-free mask blanks; however this may be difficult to achieve in practice. It is therefore essential to have strategies for inspecting mask blanks prior to patterning in order to determine whether there are any defects present on the mask blank. It is anticipated that high-throughput visible light inspection tools will be used for this purpose in a production environment; however the defects are only critical if they manifest themselves in the reflected EUV light. It is therefore necessary to determine whether there are any defects visible in the EUV that are not being detected by the visible light inspection tools in order to have confidence in the visible light inspection strategy. The purpose of the actinic inspection tool is to help answer this question.

2.1 *Bright-field and dark-field imaging modes*

2.1.1 Bright-field imaging

In bright-field mode the illumination and imaging optics are arranged such that the specular reflection component is directly captured by either the optical system (in imaging mode) or the detector (in scanning mode), and is the conventional mode in which a microscope system is operated. A schematic of bright-field imaging mode, unfolded for the sake of clarity, is illustrated in Figure 1. Subject to the limitations of the optical system, any variation in reflectivity of the mask is directly reflected in the collected image, and if the imaging system is arranged to mimic the performance of a stepper system the collected data will reflect the aerial image expected in an actual stepper system.

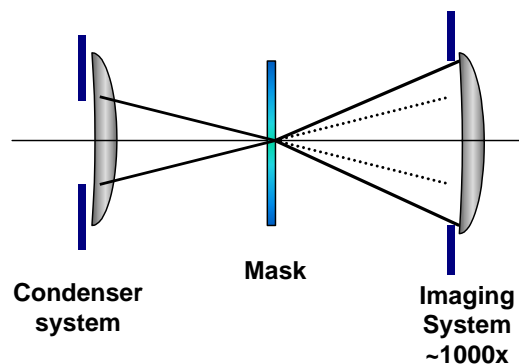


Figure 1

In bright-field imaging, the entire cone of light illuminating the mask is collected by the imaging system.

2.1.2 Dark field imaging

In dark field imaging the illumination is arranged so that the specular reflection component is not directly imaged, rather it is the light scattered by the object that is imaged. In optical microscopy this is achieved by placing an annular ring in the condenser which blocks light that would pass directly into the pupil of the imaging system as shown in Figure 2. In order to pass into the imaging system the light must be scattered by the object, resulting in an image which enhances structures such as edges which scatter light.

A similar dark-field imaging system can be employed in an EUV mask inspection system for the enhancement of feature edges by using collection optics and/or detectors which do not image the specular reflection component, and its usefulness as an actinic defect characterisation tool for EUV masks has been demonstrated by the existing actinic inspection tool at the ALS, which incorporates both dark-field and bright-field channels in the detector¹. The dark-field signal has proved particularly useful for detection of buried multilayer defects that perturb the multilayer layer structure but only weakly affect the reflectivity. At-wavelength scans of programmed defect samples have shown only a weak signal in the brightfield data due to the high background intensity, but a clear signal in dark-field mode².

¹ See, for example, M.Yi *et.al.* "High sensitivity actinic detection of native defects on EUVL mask blanks" (2001) **19**(6) J.Vac.Sci.Technol.B. 2401.

² M.Yi *et.al.* "At-wavelength inspection of defect smoothing in EUVL masks" in *Emerging Lithographic Technologies VI*, SPIE (2002).

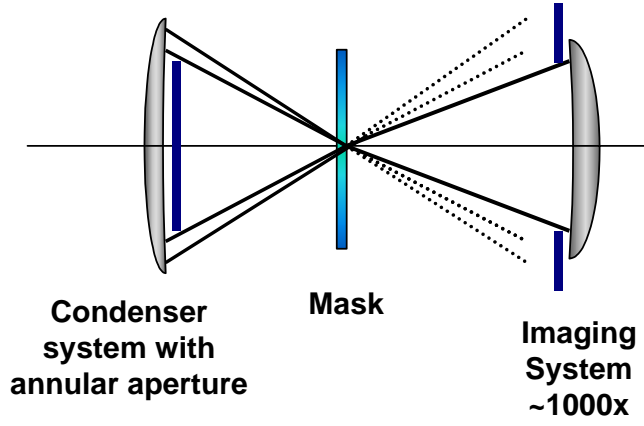


Figure 2

Schematic illustration of dark-field microscopy as employed in a transmission microscope. In reflection the system is folded back on itself around the object, but the diagram is harder to draw and more confusing to interpret.

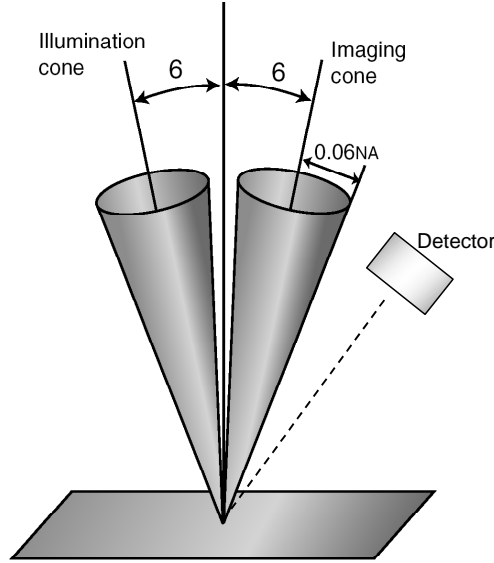


Figure 3

An example of how dark-field detection may be implemented in an AIM-mode imaging system - the specular reflection component goes into the normal imaging cone and the detector only detects light scattered from the object.

2.2 Scattering from a critical defect

The scattering cross-section of a critical defect at the 35nm node with a 0.25NA camera has been estimated to be 5000nm^2 , equivalent to a disk of approximately 80nm diameter on the mask. Whilst this figure is an approximation to the true multilayer response, we nevertheless use this as a convenient first-order estimate for assessing the expected signal from a critical defect in the scattering tool under ideal conditions.

In bright-field mode using a scanning system scattering from the defect is effectively lost from the aerial image intensity, thus the bright-field signal over the defect decreases according to the ratio of the area of the illuminated spot A_{illum} to the scattering cross-section of the defect σ :

$$I_{bf} \approx 1 - \frac{\sigma}{A_{illum}}$$

thus we see that as the illuminated spot size is made smaller the variation in bright-field intensity due to the defect increases. In the case of an imaging system in which the defect is resolved by the optical system, the field reflected from the mask is re-imaged onto a multi-element detector and the area A_{illum} is replaced by the pixel size at the mask; thus one would expect a high-magnification imaging system with a resolution comparable to the defect size to be quite sensitive to changes in bright-field intensity caused by the defect.

Turning now to the dark-field signal, if the defect causes light to be scattered outside of the pupil rather absorbed it is possible to detect this scattered light in dark-field imaging mode. In a scanning system the number of photons scattered by the defect into the dark-field is once again proportional to the size of the illuminated spot, and is given by

$$I_{df} \approx \frac{\sigma}{A_{illum}}$$

thus we once again see that the dark-field signal increases as the illuminated spot size is decreased. In theory there is no scattering from defect-free regions of the multilayer, however in practice scattering on the order of 0.5 % is typically observed from defect-free regions of the multilayer, with the scattering magnitude dependent on factors such as substrate roughness and multilayer deposition technique. There is typically a variation in dark-field signal from point to point on the level of 5-10% at spatial scales of 1 μ m or less, with the pattern being repeatable if the same region of multilayer is scanned many times. Thus the change in dark-field signal due to a critical defect has to be significantly greater than 10% in order to stand out above the intrinsic multilayer reflectivity variation. Assuming a 0.5% value for the background scattering from the multilayer on the mask, and the 5000nm² cross-section of a critical defect described above, it would be necessary to have an illuminated spot size on the order of 1.1 μ m in order for the dark-field signal from the smallest possible critical defect to vary by more than the average background scattering level of a defect-free multilayer.

2.3 Key optical system parameters

It is highly desirable that the upgraded defect inspection tool be compatible with both the first generation production tools and the MET exposure station at LBL, as this would enable inspection of standard production masks destined for either of these tools. The actinic inspection tool specifications are therefore driven by a combination of anticipated production stepper specifications, the MET specifications, and the practical requirements of both high-speed and AIM mode operation. The requirements on the optical system for AIM mode are somewhat more stringent than for defect scanning mode, therefore we discuss these first.

2.3.1 Requirements for high resolution mode

In high resolution mode, where the tool is used to provide data on defect printability, the results obtained by measuring the aerial image with the upgraded tool should, as far as practically possible, provide the same aerial image information that would be obtained in a stepper system. Mimicking the performance of a stepper, albeit over a smaller field, is therefore essential if the results obtained using an AIM tool are to provide a reliable assessment of defect printability. Production stepper optics strive to achieve diffraction-limited performance across the field, thus for an AIM tool we also desire a system capable of mimicking this diffraction limited imaging – albeit producing a magnified rather than reduced image. Probing through-focus behaviour of defects for process window analysis is one of the main applications for AIM mode, thus it is also essential that the through-focus behaviour of the AIM tool mimic that of a typical stepper system. Equivalence of the through-focus aerial image performance with that of a production system is also essential, as many types of defects manifest themselves as changes in the aerial image in through focus. Manufacturing aberrations affect both in-focus and through-focus behaviour, and therefore impact on the aerial image. Flare directly affects contrast, thus emulating the flare characteristics of a stepper system also needs to be considered when judging the equivalence of aerial image performance³.

As mentioned above, it is highly desirable that the upgraded defect inspection tool be compatible with both the first generation production tools and the MET exposure station at LBL, as this would enable inspection of masks destined for these tools. Key compatibility criterion are the numerical aperture (NA) and angle of incidence at the mask, and the wavelength of light. For the MET the angle of incidence at the mask is 4°, the NA facing the mask is 0.06 (0.3 at 5x reduction), and the wavelength is 13.5nm. The specifications for the first generation of production stepper systems is not yet fixed but it is likely that the angle of incidence will be 6°, the NA facing the mask will be 0.0625NA (0.25NA at 4x reduction), and the wavelength is likely to be 13.5nm.

It is anticipated that a commercial AIM system will be sourced for use in a production environment; whilst it would be desirable for this inspection tool to have true AIM performance, it not justified and is beyond the scope of this project to construct a custom optic capable of meeting full equivalence with the imaging quality of a stepper optic. It is therefore likely that a compromise will have to be reached in which the actinic inspection tool matches the wavelength, NA and angle of incidence of a stepper system, but suffers from a higher level of flare and performs over a smaller field of view than is desired of a full, commercial AIM tool.

³ In this regard it is important to note that it may be necessary to illuminate a larger area than the imaged field both so that the flare is uniform across the imaged field and so that flare from regions outside of the imaged field can be properly captured in the aerial image. It is possible to emulate the effect of flare in software by convolving with a flare point spread function provided the flare in AIM mode is less than that of a production stepper system.

2.3.2 Requirements for high-speed scanning mode

For high-speed scanning mode the goal is to scan a large area of unpatterned mask blank looking for defects in the multilayer coating. Speed is essential as the defect density is anticipated to be low – of the order of 0.05 defects/cm² or one defect in every 20cm² (on average). In order to obtain sufficient statistics to determine whether visible light scattering tools are seeing all relevant multilayer defects it will be necessary to scan several hundred square centimetres of mask blank, thus high speed operation of the tool is critical.

As described above, a defect is any area on the mask that causes unwanted variation in the dose of the aerial image. This is commonly caused by either absorption of the EUV in a defective multilayer coating or the scattering of light outside of the acceptance angle of the stepper projection optics. Any drop in intensity can be determined by measuring the specular multilayer reflection directly using, for example, a photodiode. However, small defects produce only a very small change in this bright-field signal and are therefore difficult to detect compared to system noise sources.

To date the highest sensitivity for EUV defect detection has been obtained in dark-field mode where only the light scattered out of the entrance pupil is detected. There is background scatter from the multilayer of the order of 0.5% to 1% above which the dark-field signal from a defect must rise in order to be registered as a defect – and this sets a theoretical bound on the signal to noise ratio obtainable in dark-field imaging mode. Note also that dark-field imaging is insensitive to absorption-only defects, thus it is desirable to include capacity for both bright-field and dark-field detection in the scanning mode implementation.

The optical system specifications are set by the goal of making the system compatible with masks destined for either the MET or production tools. Unlike AIM mode, where emulation of stepper imaging characteristics is essential, for defect scanning it is not critical that the bandwidth, angle of incidence or NA facing the mask match that of a production stepper system, thus there is greater flexibility in selection of these values to suit system design constraints.

2.3.3 Summary of target specifications

Following on from the above discussion, we identify the following key specifications and requirements for the upgraded actinic mask blank inspection system:

	High resolution mode	Defect scanning mode
Wavelength	13.5nm	13.5nm
NA	0.0625NA	TBD
Angle of incidence	6°	TBD
Bandwidth	TBD	TBD
Resolution limit	107nm	≈1μm (TBD)
Pixel size at mask ⁴	$\Delta x < 53\mu m$	≈1μm
Field of view ⁵	10x10μm or better	Scan-dependent
Throughput	<10s per exposure	1cm ² /hr or better
Physical size ⁶	Preferably 1x1x2m or smaller to fit at BL11.3.2	Integrated in same unit

Table 1

Key specifications and requirements for an EUV AIM tool in AIM and both high-resolution modes.

⁴ A factor of 2 better than the spatial resolution is required for adequate sampling in imaging mode. This requirement is more relaxed in scanning mode where scattering from a defect simply has to be located rather than imaged.

⁵ This is a suggested target value. The actual field of view and size of the field of view may result from a performance and design compromise.

⁶ The main requirement is that the unit fit at the BL11.3.2 end-station space available at the ALS.

2.4 Selection of beamline

The existing system on beamline 11.3.2 uses a bending magnet source and is currently dedicated to the EUV inspection project. Beamline 11.3.2 has an identical front-end to the calibration and standards system on beamline 6.3.2, consisting of a pair of grazing-incidence mirrors, a monochromator and a set of filters. This bend magnet source has a theoretical flux of 10^{11} photons/second/0.01% bandwidth at 100eV available after the monochromator and first K-B mirror pair, and measurements at beamline 6.3.2 confirm a flux of approximately 0.8×10^{11} photons/second/0.01% bandwidth at 100eV.

One of the factors that limit scan speed is available photons. A certain number of photons must be detected in order to maintain a given signal-to-noise ratio, thus the maximum scan speed is in part determined by available flux. One option for improving flux is to move the system to an undulator beamline, for example beamline 12.0 where the MET and EUV interferometry station is to be located. On this beamline the available flux is of the order of 10^{13} photons/second/0.01% bandwidth at 100eV, a factor of 100 higher than at beamline 11.3.2, and the increased coherence of an undulator source enables a tighter focus to be formed further increasing throughput through the pinholes. However, beamline 12 is in high demand and can not be dedicated to the EUV inspection project; in fact beamtime on 12.0 is currently fully booked for all of 2003, thus moving the inspection system to beamline 12 poses significant problems in terms of access to beam from the ALS. Space is also a concern, as there are many projects sharing beamline 12.0, leaving little room for introducing an inspection project. This is further complicated by the requirement of some form of cleanroom for the mask inspection project, an item which would take up significant space.

In the light of these anticipated difficulties with moving to beamline 12.0 it has been decided to try and retain the project on beamline 11.3.2 if possible where we have dedicated access to light from the ALS and we can run the tool 24/7 if required. Moving to another beamline will only be considered if it is unlikely that beamline 11.3.2 will satisfy the needs of this project. We will also aim to retain the front-end of the current beamline, up to the pinhole chamber, in order to minimise the amount of modification required to the beamline itself.

3 Overview of candidate systems

In this section we provide a brief top-level examination of several candidate optical systems with a view to selecting one or at most two systems for more detailed investigation. Being able to efficiently scan large areas of mask blank is essential for this project, thus at this stage we focus on fundamental limitations on system throughput and sensitivity so as to select a system which will have the highest possible scan rate. We also briefly discuss technical limitations and risk items that may limit the performance of each system.

3.1 Existing system using grazing incidence Kirkpatrick-Baez optics

The existing defect inspection system at the ALS uses a set of grazing incidence mirrors aligned in the Kirkpatrick-Baez (K-B) configuration to re-image a pinhole onto the mask. Using a $25\mu\text{m}$ pinhole, the K-B mirrors form a $3 \times 5\mu\text{m}$ spot on the mask, which is raster scanned to look for defects. Light scattered from the mask is detected in bright-field by a photodiode and in dark-field by specular and scattered beam reflected from the mask.

The pinhole is illuminated by the ALS beam from a bending magnet source, which is focussed into a $100 \times 300\mu\text{m}$ elliptical spot in the pinhole plane by set of grazing incidence Kirkpatrick-Baez mirrors as illustrated in Figure 4. The front-end of this system, from the storage ring to the pinhole, is identical to that on the beamline 6.3.2 (Calibration and Standards) system where a flux of 0.8×10^{11} photons/second/0.1% bandwidth has been measured at the pinhole plane (first K-B focus).

A schematic of the current beamline layout is shown below.

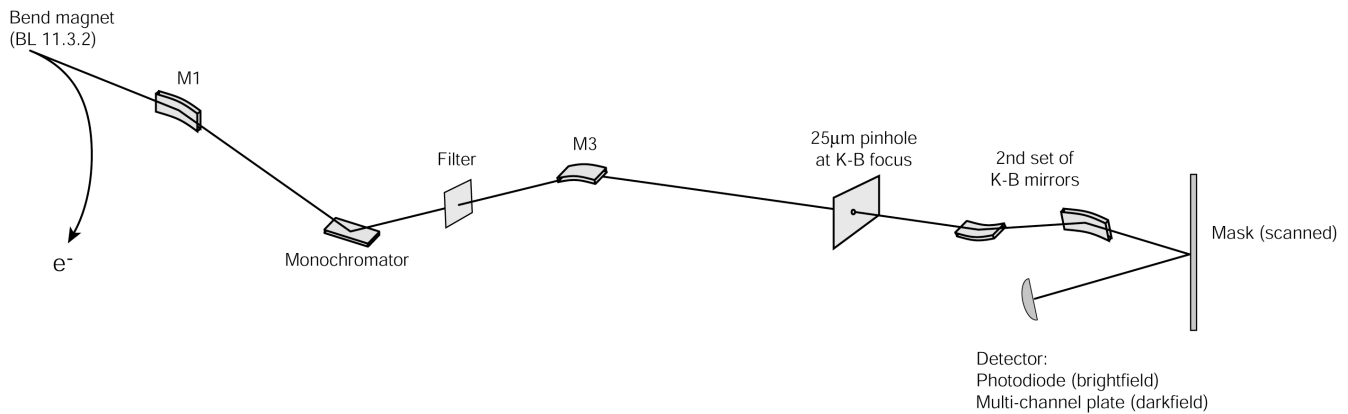


Figure 4

Schematic layout of the existing defect inspection system at ALS beamline 11.3.2.

This system has been adequate to date, and given the resources devoted to the project at the time. However there are several factors that limit the performance of this system given the throughput and spatial resolution goals of this project:

3.1.1 Resolution limit

The minimum spot size available at the mask is set by the magnification system used, in particular the NA and aberrations of the focussing optic. The existing grazing incidence K-B mirror pair has a low numerical aperture (NA) that limits the spot size on the mask to $\approx 3 \times 2 \mu\text{m}$. This is larger than desired for obtaining a good signal-to-noise ratio for critical defects at the 35nm node. It is also inadequate spatial resolution for operation as a scanning high-resolution microscope where 100nm resolution with 50nm step sizes on the mask is desired.

3.1.2 Angle of incidence

The angle of incidence at the mask is 10° , which does not match that anticipated for production stepper systems nor the MET. Whilst this might not be a significant concern for high-speed defect scanning, issues of shadowing become important in high-resolution mode where more detail of the defect structure is desired. In particular, if the system is to be used as a microscope for inspecting patterned EUV masks it is essential that the angle of incidence match, or at least be closer to, that anticipated for lithographic tools so as to avoid any doubt about the effect of shadowing on the collected image.

3.1.3 Scanning stages

The existing Parker-Daedal stages are not fast enough for high-speed scanning and do not have sufficient precision for operation in high-resolution scanning microscope mode. Whilst the Heidenhain encoders on the current system are accurate to $0.1 \mu\text{m}$, the existing stage mechanism does not support such precise motion. Speed is also a limiting factor. The current stages can run at up to 3cm/sec in an x-y scan pattern, but higher speed scanning is desired in order to improve system throughput. A stage upgrade in some form is therefore required to support both high-speed and high-resolution operation.

3.1.4 Vibration

Practical experience with the current beamline indicates that strong coupling of acoustic vibration into the optical system produces variation in the measured signal, limiting sensitivity and necessitating the averaging of many data points in order to reduce noise effects. Floating the detection chamber on isolation supports, as done for optical tables, is not a practical option due to the requirement of maintaining alignment with the ALS beam (the location of which is theoretically fixed with respect to the floor). Whilst floating the entire bench may not be practical, constructing the entire system on an optical table should reduce noise significantly: the X-ray microscope XM-1 on beamline 5 is built on a commercial optical table and routinely obtains spatial resolution of 25nm or better.

3.2 *Scanning system with 10x optics*

A 10x Schwarzschild camera modified to operate at 20x magnification to maximise flux incident on the mask replaces the existing K-B optics in the current system. The superior NA and optical performance budget of the 10x camera

compared to grazing incidence K-B mirrors enable a smaller spot to be produced on the mask, increasing both spatial resolution of the inspection system and the signal-to-noise for measurement of scattering from a defect. As with the existing system the mask is scanned to search for defects and build up an image of the mask.

A conceptual schematic of the beamline with the K-B optics replaced by a 10x camera is shown in Figure 5 below:

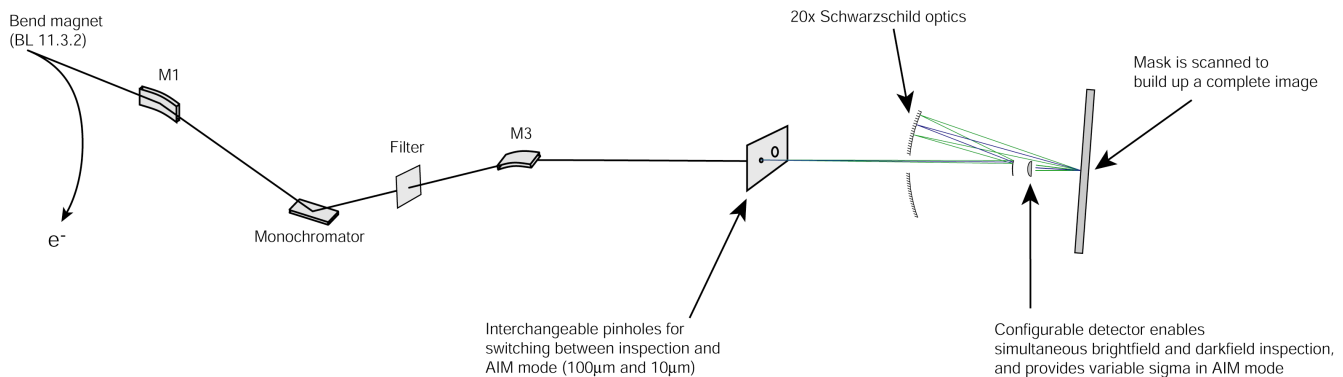


Figure 5

Upgrade to the existing beamline using 10x Schwarzschild optics.

There are several key system issues associated with this design that we investigate below:

3.2.1 Increased flux obtained by removing the monochromator

The bandwidth of the current system is 0.1%, which is set by the monochromator design and exit slit width. Using a 10x camera enables the monochromator to be replaced with a mirror blank, with wavelength selection performed by multilayer-coated optics (either on the Schwarzschild camera or in a fold mirror). The bandwidth of a two-reflection multilayer system is approximately 2%, giving an immediate increase in available in-band flux at the mask of approximately 20x over a monochromator operating at 0.1% bandwidth, enabling higher speed scanning for the same system noise level. It is necessary to retain a Be or Al filter in the beamline, at the expense of a 50% in-band throughput hit, to block out-of-band radiation because out-of-band components of the ALS beam will reflect off both the 10x optics and the mask and will be detected as a strong background signal if they are not blocked.

3.2.2 4x throughput gain in moving from 10x to 20x magnification

We propose to modify the 10x optics to operate at 20x magnification in order to increase flux through the system by the use of a larger pinhole. For a given spot size upgrading the magnification from 10x to 20x doubles the size of the pinhole, increasing throughput by 4x. The change from 10x to 20x magnification can be performed comparatively easily by changing conjugate planes: the distance from object to image planes increases from 313mm at 10x to 573mm at 20x, and the mirror spacing is decreased by 650µm. There is some risk in moving to a 20x system: whilst it is simple to modify the housing for operation at 20x magnification, the existing alignment hardware will have to be modified for alignment of a 20x system.

3.2.3 Gain in signal-to-noise through reduction of the spot size

Moving to a smaller spot size increases the flux per unit area on the mask, increasing the relative strength of scattering from a defect compared to scattering from background multilayer and thereby improving detection sensitivity. However using a smaller spot size also necessitates moving the sample in finer steps so as to ensure coverage of the whole mask, which requires an increase in sampling rate (measurements per second) to ensure that scan speed does not suffer.

In order to detect a defect the EUV light scattered from a defect must stand out against sources of background noise. Assuming system noise levels can be controlled the main source of noise in the darkfield signal is scattering from the multilayer. As discussed previously the scattering from a critical defect is estimated to be of the order of 5000nm², whilst scattering from the multilayer itself is typically of the order of 0.5% of the incident signal, giving a suggested spot size of 1.1µm diameter or smaller for reasonable signal-to-noise in scanning mode operation.

Reducing the spot size even further to increase sensitivity comes at the expense of loss of photons (through use of a smaller pinhole) and increased scanning time (because the smaller spot has to be scanned across the mask at higher resolution).

3.3 Scanning system with zone plate optics

One way to increase the system magnification, and therefore the size of the pinhole that can be used, is to replace the 10x optic with a high-magnification zone plate lens. Moving to a higher magnification system enables some of this lost throughput to be recovered through the use of larger pinholes. Zone plate lenses are relatively easy to fabricate and, due to the typically short focal lengths, are ideally suited for use in a high-magnification system.

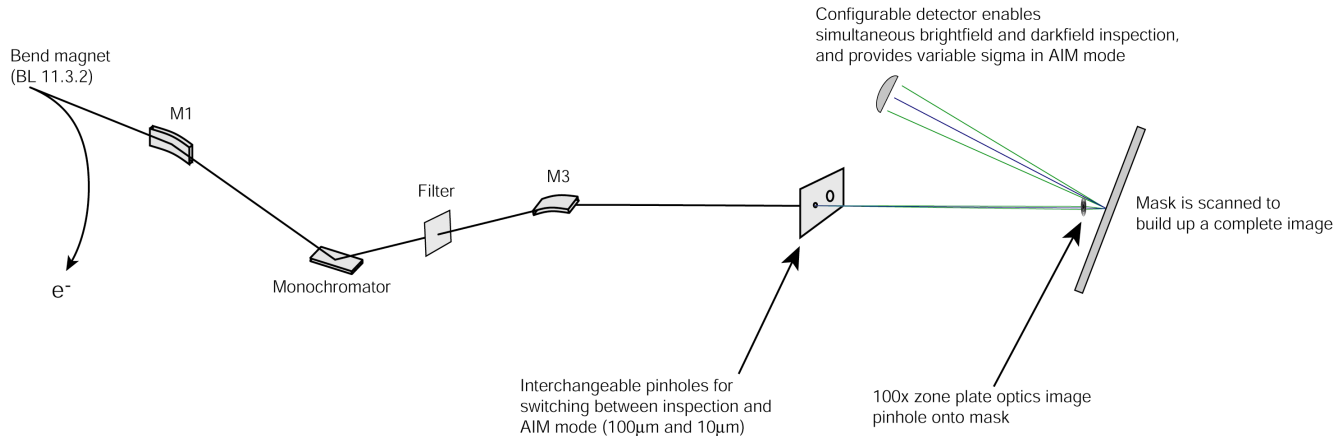


Figure 6

Upgrade to the existing beamline using a high magnification (100x) zone plate lens to image a pinhole onto the mask.

The basic principle of operation is identical to that for the 10x scanning system – the mask is scanned under the focal spot formed by imaging a pinhole onto the mask using a demagnifying optic, which is in this case a 100x zone plate lens. The pinhole is illuminated by the first set of K-B optics, and for the case of a 100x zone plate lens can be 100 μ m in diameter to produce a 1 μ m spot size, giving a factor of 25 increase in transmitted flux over the 20 μ m pinhole proposed for use with the Schwarzschild camera design. For high-resolution mode the pinhole size is reduced to 10 μ m, producing a 100nm spot on the mask for use in high-resolution mode.

There are, however, several technical downsides to the use of a zone plate lens that have to be balanced against the possible throughput gains. These include:

1. Flare. Zone plate optics are known to suffer from flare as a result of small zone placement errors. This flare will serve to increase the background signal level, making the signal from a defect somewhat harder to detect. With careful zone plate fabrication, however, the level of flare may be manageable.
2. Bandwidth. Zone plate performance suffers from a high degree of chromatic aberration. This is because the optics operate by diffracting light from regular, physical structures, and diffraction is a wavelength-dependent effect. The bandwidth which must be accommodated by a zone plate determines the number of zones that can be used, and for a zone plate of practical dimensions
3. Image quality. Anticipated quality of AIM mode imaging will require careful analysis, and the use of a scanning system for high-resolution mode will make stage selection a key issue.

These questions will have to be resolved only if the system throughput proves to be superior to other solutions, so a detailed discussion is deferred until later.

3.4 Zone plate imaging system

The conceptual design for a defect inspection system based on imaging the mask is sketched Figure 7 below. In this system an extended region of the mask is illuminated with the primary focus of the first K-B optics; this illuminated patch is imaged onto a CCD using a zone plate microscope enabling the simultaneous inspection of up to 2000x2000 pixels of mask surface. This system therefore has the initial attraction of leveraging massively parallel detection and the absence of flux-limiting pinholes to boot overall throughput.

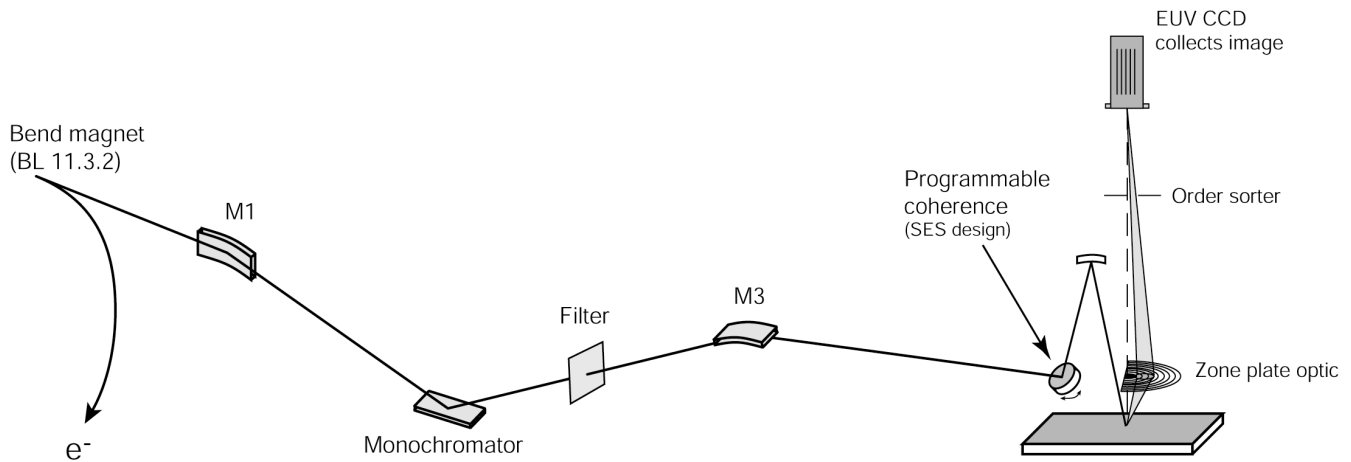


Figure 7

Mask inspection system based on imaging the mask with a zone plate microscope operating at 300x magnification. A large area of the mask (100x100 μm square) is imaged at a time, improving throughput.

The basic idea behind this system is to have a zone plate microscope image the mask onto a CCD at a magnification of approximately 300x. For defect scanning, the system would be run as a dark-field microscope, with the illumination directed onto a central stop on the zone plate. Thus only the dark-field scattering signal would be imaged onto the CCD for defect detection. In imaging mode, the illumination would be altered so as to bypass the central stop, converting the microscope into a conventional, brightfield microscope for imaging the mask (including patterned masks). This change could be implemented efficiently if a programmable coherence system is included in the design (as is actually required to get decent imaging out of the system in brightfield mode).

A full-field imaging system requires an area detector such as a CCD in order to detect the image rather than a single photodiode as in a scanning system. CCD cameras for operation at EUV wavelengths (13.5nm or 92eV) are readily available with pixel sized down to 13.5 μm in array sizes up to 2048x2048 pixels (for example an EEV 42/40 CCD chip in Princeton Instruments PI-SX camera housing available at a cost of \$60k). A magnification of 300x combined with a CCD with 13.5 μm pixels produces 45nm pixels on the mask (or 4 pixels per linewidth at the 45nm node), and this magnification can be readily achieved with a zone plate microscope. There is an existing fabrication and user base for zone plates at the ALS, which helps reduce the risk involved in adopting this approach.

Some form of partial coherence control will be required on this system, thus we have included a system akin to the SES programmable coherence unit in our design. The beam divergence at the focus of the first set of K-B mirrors is of the order of 1.8x4.3mrad, corresponding to a pupil fill of $\sigma=0.02\times0.06$ into a 0.0625NA entrance pupil. Using the K-B focus with no coherence control measures would therefore give effectively coherent imaging and not satisfy the requirements of stepper-equivalent imaging in high-resolution mode.

Two key issues for this type of system are throughput and available detection modes. In high-speed defect inspection mode it is likely that the imaging rate will be limited by the CCD frame rate.

If we peg the image acquisition time at 1sec per exposure and image a 100x100 μm square patch of mask at a time scan rate is 2.7hrs/cm². This still enables the inspection of one mask blank in just over one week of inspection time, which may be adequate for the proposed defect cross-correlation experiments. However it is also not significantly higher than the current scanning rate of approximately 5hr/cm² – the key advantage gained in upgrading via this path is the ease with which the system can be converted to a bright-field imaging microscope. By simply changing the illuminator configuration the microscope can be converted from a dark-field inspection system to a high-resolution bright-field microscope, a capability not available on the current inspection system.

Of greater concern is the fact that this type of imaging system is incompatible with simultaneously detecting bright-field and dark-field channels. The illumination has to be adjusted to change between modes, thus it would be necessary to image each region of the mask twice in order to collect both signals. In the current scanning system greatest sensitivity to buried defects has been observed in the darkfield channel, however it was also observed that some defects manifested themselves primarily in the brightfield channel with little associated darkfield scattering. Simultaneous data collection is therefore desirable to capture all types of defects.

3.5 *Comparative analysis of throughput rates*

A key performance measure for the current project is system throughput in terms of area of mask inspected per hour. High throughput is required in order to ensure that sufficient area of mask blank can be inspected in a reasonable time to determine whether actinic inspection is required for EUVL. We therefore proceed to estimate the system throughput rates for the abovementioned systems in order to ensure that the candidate selected meets required performance criteria. It is also useful to compare these throughput budgets to the current system so as to verify that the proposed upgrade represents an improvement on current system performance of up to 5hr/cm² throughput just prior to being shut down.

What follows is a spreadsheet containing estimates of key system performance parameters, leading to an overall estimate of anticipated system throughput rates for each different configuration based primarily on photon flux and signal-to-noise issues.

3.5.1 Projected throughput and scan rates of the candidate systems

Preliminary calculation of system throughput rates		Units	Scanning Existing K-B	10x Scanning		Zone plate scanning		Zone plate Imaging	
				High speed	High-res	High speed	High-res	High speed	High-res
Source parameters									
(at 1st K-B focus)									
Number of photons per second at KB focus, 0.1%BW		/sec	1.00E+11	1.00E+11	1.00E+11	1.00E+11	1.00E+11	1.00E+11	1.00E+11
Actual bandwidth			0.1%	2.0%	2.0%	0.1%	0.1%	0.1%	0.1%
Number of photons per second at KB focus in used bandwidth			1.00E+11	2.00E+12	2.00E+12	1.00E+11	1.00E+11	1.00E+11	1.00E+11
Vertical dimensions of spot at focus		um	100	100	100	100	100	100	100
Horizontal dimensions of spot at focus		um	300	300	300	300	300	300	300
Area of spot at focus (ellipse)		um^2	23633	23633	23633	23633	23633	23633	23633
Vertical divergence at focus		mrad	4.36	4.36	4.36	4.36	4.36	4.36	4.36
Horizontal divergence at focus		mrad	1.85	1.85	1.85	1.85	1.85	1.85	1.85
Key optical system parameters									
Magnification		x	10	20	20	100	100	250	250
Parent NA						0.166	0.166	0.166	0.166
Outer zone width		nm				40.7	40.7	40.7	40.7
Number of zones to match bandwidth						1000	1000	1000	1000
Number of zones actually used on zone plate						2000	2000	2000	2000
Focal length		um				980	980	980	980
Zone plate diameter		um				325	325	325	325
Track length for given magnification		m				0.10	0.10	0.24	0.24
Diameter of useable field of view (approx D/3)		um				108	108	108	108
CCD parameters									
CCD pixel size		um						13	13
Number of pixels square								2048	2048
Pixel binning								4	1
Pinhole losses									
Pinhole size (diameter)		um	25	20	2	100	10		
Transmission through pinhole			2%	1.33%	0.013%	33%	0.33%		
Diffraction divergence after pinhole (2*1.22*w/d)		mrad	1.3	1.6	16.5	0.3	3.3		
Vertical divergence after pinhole		mrad	4.36	4.36	16.47	4.36	4.36		
Horizontal divergence after pinhole		mrad	1.85	1.85	16.47	1.85	3.29		
Pupil fill									
Divergence from pinhole subtended by pupil plane		mrad		13	13	1.11	1.11		

Preliminary calculation of system throughput rates		Units	Scanning Existing K-B	10x Scanning		Zone plate scanning		Zone plate Imaging	
			High speed	High-res	High speed	High-res	High speed	High-res	
Bright field detector									
Number of photons we need per pixel at detector			1000	1000	1000	1000	1000	1000	1000
Shot noise level		%	3%	3%	3%	3%	3%	3%	3%
Available photons per second at given noise level			7.3E+08	5.2E+07	7.9E+07	4.4E+05	6.9E+02	4.3E+01	
Measurements per second at given noise level		Hz	732667	8169404	52475	444	0.689	0.043	
Actual number of measurements pre second, given potential data rate			100000	100000	52475	444	0.689	0.043	
Area imaged per second at normal step size		um^2	490781	78525	412.06	3.49	7817	489	
Area imaged per second at 50nm step size		um^2	250	250	131.19	1.11	452	452	
Dark field detector									
Number of photons we need scattered from defect per pixel at detector		#	200	200	200	200	200	200	200
Shot noise level		%	7%	7%	7%	7%	7%	7%	7%
Number of photons available per pixel			7.33E+08	5.25E+07	7.91E+07	4.44E+05	6.89E+02	4.31E+01	
Scattering cross-section of critical defect at 0.25NA		nm^2	5000	5000	5000	5000	5000	5000	5000
% of photons incident on one pixel scattered from an isolated defect			0.10%	63.67%	0.64%	63.67%	11.56%	100.00%	
Number of photons scattered from an isolated defect into one pixel		/sec	7.46E+05	3.34E+07	5.04E+05	2.83E+05	7.97E+01	4.31E+01	
Background scattering from multilayer roughness			0.5%	0.5%	0.5%	0.5%	0.5%	0.5%	0.5%
Number of photons scattered from multilayer into one pixel		/sec	3.7E+06	2.6E+05	4.0E+05	2.2E+03	3.4E+00	2.2E-01	
Background scattering level from optics			0.0%	0.0%	0.0%	0.0%	1.0%	1.0%	1.0%
Number of photons contributed from optical system scattering			0.0E+00	0.0E+00	0.0E+00	0.0E+00	6.9E+00	4.3E-01	
% change in darkfield signal due to an isolated critical defect			20%	127%	127%		770%		
Measurements per second at given noise level		Hz	3732	260089	2519	1414	0.40	0.22	
Area imaged per second		um^2	18317	204235	1978	11	4517	2443	
Scan rate									
Brightfield imaging rate at 50nm step size (mm^2/hr)			0.900	0.472273	0.7120	0.003999	1.626	1.626	
Time to scan a 100x100um square patch at 50nm step size		min	0.67	1.27	0.84	150.05	0.37	0.37	
Number of 100x100um patches per minute at 50nm step size		/min	1.50	0.79	1.19	0.01	2.71	2.71	
Darkfield scan rate (cm^2/hr)			0.659	0.0472273	0.07120	0.0003999	0.163	0.088	
Hours to scan 100cm2 in darkfield mode		hr	152	14	1405	250086	615	1137	

3.5.2 Comparison of dark-field defect scanning speed

For defect inspection mode high-speed performance in dark-field scanning mode is critical in order to cover as large an area of mask blank as possible in a reasonable time. We therefore seek the system that is least photon-limited of all the candidate systems evaluated above. Figure 8 shows a comparison of the projected scan rates for each system based on photon flux and signal-to-noise limitations.

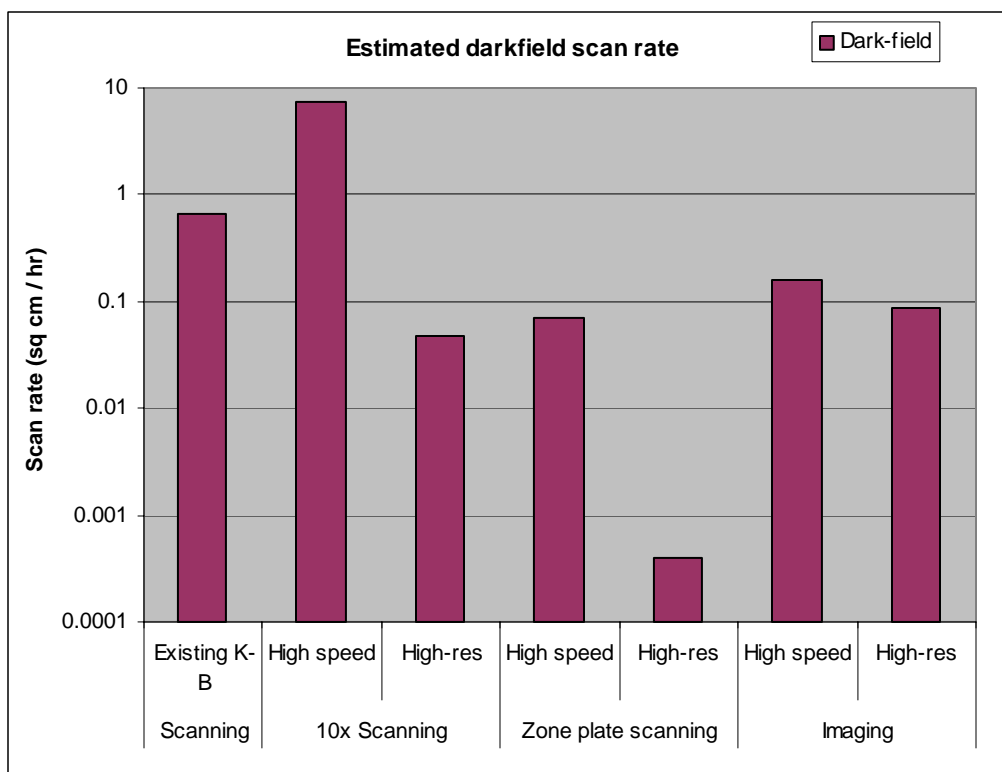


Figure 8

Estimated darkfield scan rates based on throughput calculations.

Key points relevant to each system are as follows:

3.5.2.1 K-B system

The current implementation in which scan speeds of 5hr/cm² were achieved. The theoretical throughput rate can be increased through the use of white light synchrotron radiation, in which case the mask is the first bandwidth-limiting item in the optical chain. Even with more flux, the spot size limitation of this system limits the sensitivity to a 20% change in dark-field signal due to the presence of a critical defect once the effect of background multilayer scattering is taken into account. Slower speed scanning is therefore required to ensure sensitivity to this small fluctuation in dark-field signal.

3.5.2.2 10x system

High-performance is obtained in dark-field mode through use of full multilayer bandwidth. The use of a small (1μm diameter) spot size yields a 120% change in darkfield signal for a critical defect. Data acquisition rate required to support this scan speed is 260kHz per channel of data.

3.5.2.3 Zone plate scanning system

The requirement to retain the monochromator in a zone plate design and the comparatively low throughput of a zone plate limit available photon flux, even though higher magnification enables the use of a larger pinhole. The anticipated change in dark-field signal due to a critical defect is similar to that of the 10x scanning system due to use of a similar spot size at the mask.

3.5.2.4 Zone plate imaging system

Offers parallel detection of many pixels at one time, and gains flux by dispensing with the requirement to use a pinhole. However the requirement to retain some form of monochromator for the zone plate and the relatively low throughput of the

zone plate optics limit the potential throughput rate. Of concern is that this system is only capable of detecting in dark-field or bright-field mode at a time, limiting the ability to simultaneously scan for bright-field only and dark-field only defects.

3.5.3 Comparison of bright-field imaging speed

For operation as an actinic mask inspection microscope performance in high-resolution bright field imaging mode with 50nm pixel sizes on the mask is critical. Scanning large areas of mask blank is not required, however it is useful to have as high a throughput rate as possible so as to be able to efficiently inspect a mask. If use input is required during imaging, near real time imaging capability would be preferred. The need to scan only a small region of the mask effectively precludes the use of a circular scanning pattern in which the mask is rotated under the imaging spot. Rather, it is more efficient to implement an x-y raster scan over a small (100x100 μ m) region of the mask. Figure 9 shows a comparison of the projected scan rates for each system based on photon flux and signal-to-noise limitations.

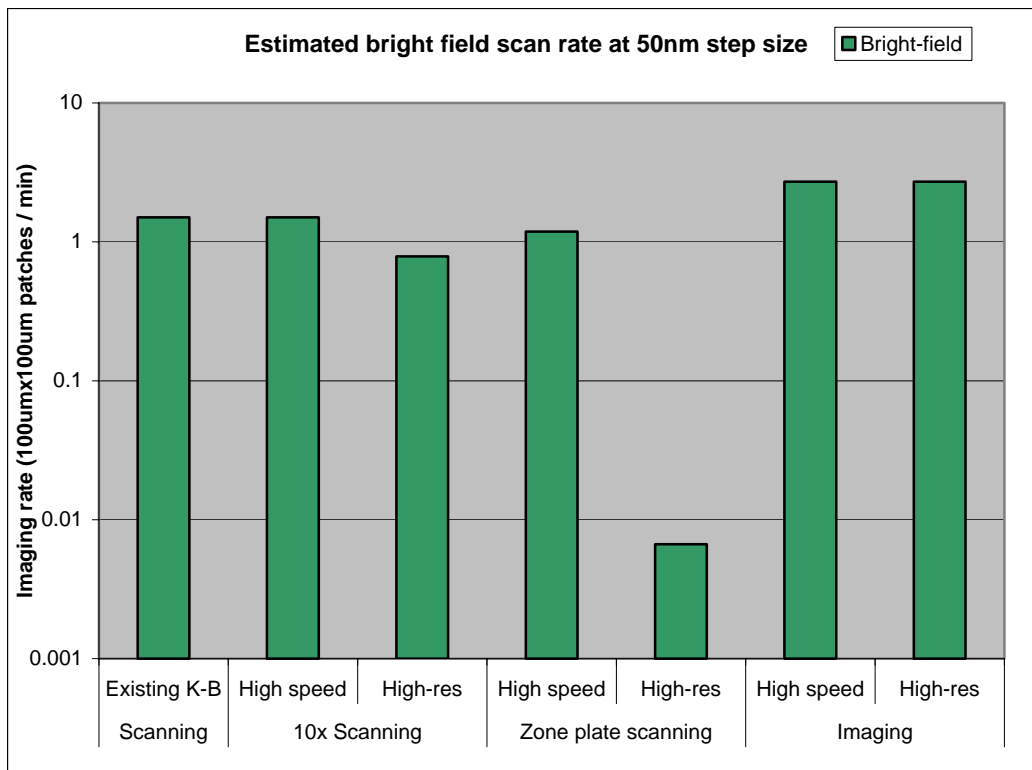


Figure 9
Estimated bright-field scan rates in high-resolution mode based on throughput estimates

Key points relevant to each system are as follows:

3.5.3.1 K-B system

The resolution limit of the current K-B imaging system is of the order of 2x4 μ m, which is insufficient for obtaining stepper-equivalent imaging at the mask. Whilst a stage upgrade may allow 50nm step sizes, the optical resolution of this system simply would not support stepper resolution imaging of the mask.

3.5.3.2 10x system

The diffraction-limited resolution of the 10x optics is 100nm, which is adequate to support stepper resolution imaging on the mask if the pinhole size is reduced to 2 μ m diameter. However, this comes at the expense of a 100x loss in flux through the pinhole, which translates directly into optical system throughput. The scan speed then becomes photon-limited rather than digitisation limited if the system digitisation rate is pegged at 100kHz. An upgrade to translation stages with absolute accuracy better than 50nm would be required.

3.5.3.3 Zone plate scanning system

As with dark-field scanning, the requirement to retain the monochromator in a zone plate design and the comparatively low throughput of a zone plate limit available photon flux, even though higher magnification enables the use of a larger pinhole. We do not anticipate that this system would be competitive for high-resolution inspection mode.

3.5.3.4 Zone plate imaging system

The zone plate imaging system is based on the paradigm of the XM-1 soft X-ray microscope for biological imaging installed at the ALS, adapted for use in mask inspection. The system is highly efficient and users of XM-1 can typically walk away with over 600 high-quality images a day. Whilst not directly adaptable for use in defect inspection, adding this capability to the mask inspection system would greatly increase the practical uses of the upgraded defect inspection system to include the inspection and review of patterned masks rather than just the inspection of unpatterned mask blanks. High-throughput comes from obviating the need to use a pinhole for high resolution. As a full-field image can be acquired in a matter of seconds the system provides near real-time user feedback, whilst the capture of frames of data relaxes the requirements on absolute stage precision whilst in motion and allows some 'hunting' for defects if required. With the acquisition of 50x50 μm frames of data in a matter of seconds, defects need only be located to within the order of microns in order to be captured within a single bright-field image.

4 Preliminary system design

4.1 Baseline system description

The current prototype at-wavelength inspection system is based on scanning the mask blank under a focused EUV beam, looking for change in specular reflectivity (bright field) or in off-specular scattering (dark field) intensity⁷. In the current scanner, the spot size achieved is 2.5 by 4 μm when a 10 x 30 μm aperture is used. The term area demagnification factor is introduced to describe the ratio of the object pinhole area to the beam area. In the current case, the area demagnification is 30. The general schematic of the system is given in Figure 10. In Figure 10 (a), the beamline construction is shown and in Figure 10 (b) the close-up view of the scanner is shown. The M1 mirror produces a 1:1 horizontally focused image of the synchrotron source onto the centre of the pinhole chamber and M3 images the exit slit of the monochromator onto the centre of the pinhole chamber. The grating in the monochromator has a grating with 200 lines/mm and the resolving power is 1/730 with the exit slit width of 100 μm . As a result, the spot size measured at the centre of the pinhole chamber is 300 μm (Horizontal) by 100 μm (vertical). The focusing optics in the scanner makes an image of the pinhole inside the pinhole chamber and produces the focused spot on the sample. The throughput of the focusing optics (from point A to point C) is estimated to be 32% assuming 80 % transmission from the two glancing angle mirror (from point B to point C) and 40 % transmission through the quad alignment apertures (from point A to point B). If the sample reflectivity is assumed to be 60%, the ratio of the number of photons from point A to point D is 19.2 %.

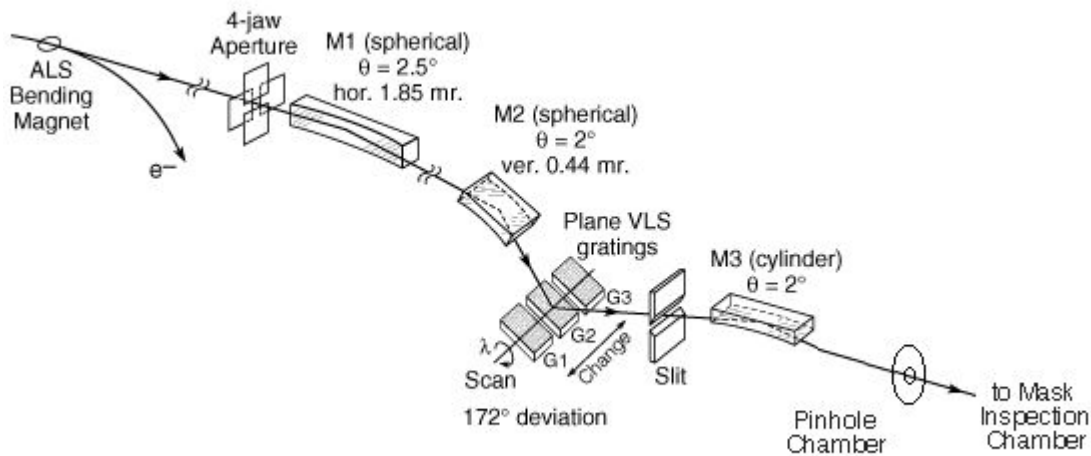


Figure 10(a)

Schematic of the beamline 11.3.2 at Advanced Light Source. Original picture provided by E. M. Gullikson and J.H. Underwood.

⁷ S. Jeong, M. Idir, Y. Lin, L. Johnson, S. Rekawa, M. Jones, P. Denham, P. Batson, R. Levesque, P. Kearney, P. Yan, E. Gullikson, J. H. Underwood, J. Bokor, "At-wavelength detection of extreme ultraviolet lithography mask blank defects", *Journal of Vacuum Science & Technology B*, **16**(6), 3430-3434, Nov-Dec, 1998.

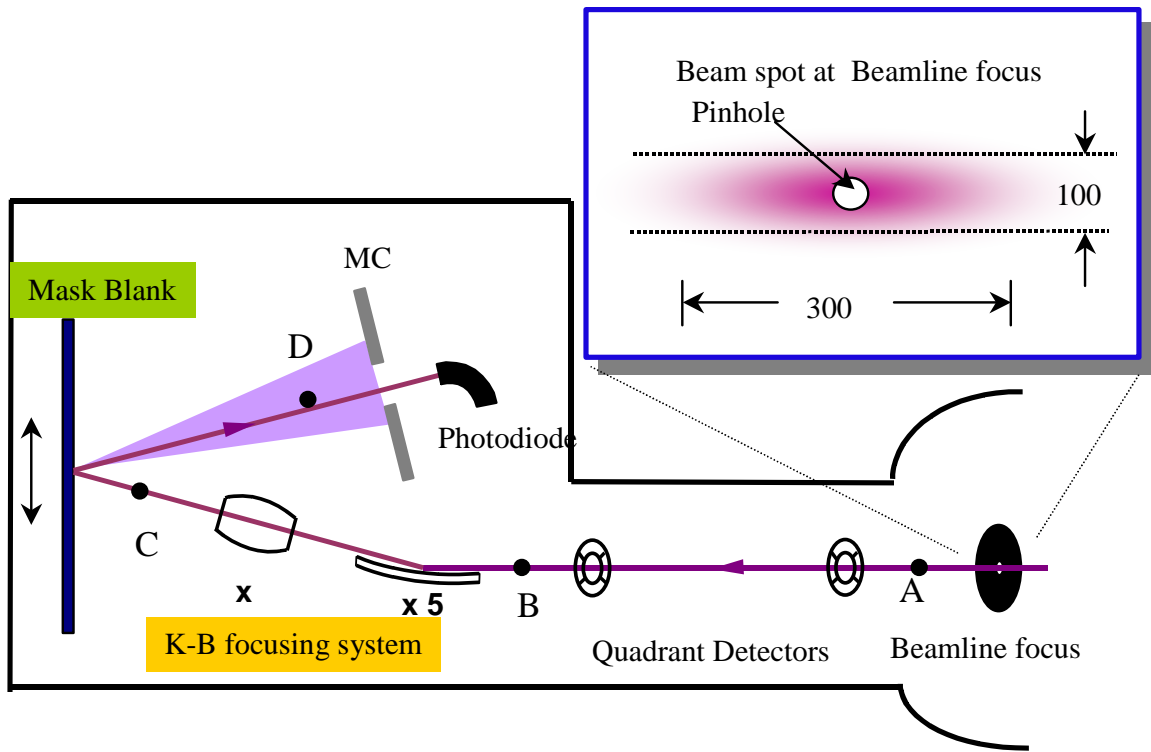


Figure 11(b)
Schematic representation of the mask inspection chamber.

4.1.1 Estimate of scanning time

In this scanning scheme, the total amount of time for inspection is $N_p T_p$, where N_p is the number of pixels per unit area and T_p is the dwell time per pixel. N_p can be obtained from the unit area divided by the size of a single pixel. Typically, the size of a single pixel is chosen to be a fraction (typically 0.3) of "beam area". The reason for this choice is to make the *effective pixel size* equal to the beam size and oversampling to reduce the number of false alarms. For example, if the beam size is $2.5 \mu\text{m}$ by $4 \mu\text{m}$, i.e. $10 \mu\text{m}^2$, as in the current scanner, the pixel size is usually chosen to be $3 \mu\text{m}^2$ (0.75 by $4 \mu\text{m}$) and there are thirty three million pixels per 1 cm^2 . The dwell time, T_p , is set to achieve an adequate signal to noise ratio for detecting defects of certain size, typically 100 nm .

4.1.2 Signal strength from defects.

The signal strength from a defect generally scales with the ratio of the defect footprint to the beam footprint. For example, the bright field signal shows 1 % signal for 100 nm defect when the beam footprint is $1 \mu\text{m}^2$ and 0.1 % when the beam footprint is $10 \mu\text{m}^2$ in size⁸. The dark field signal contrast is rather complicated to estimate because it depends more on the nature of the defect as well as the lateral size. Also the dark field has a finite background due to scattering of EUV photons from the roughness in the multilayer. Therefore, the extra scattering from the defect appears as a peak against a constant background. Unfortunately, the level of background varies from sample to sample and it varies depending on the processing condition such as patterning. It is generally expected that a multilayer bump resulting from a substrate defect and subsequent conformal multilayer deposition displays a stronger signal than a defect of the same size but located on top of the multilayer. From experimental data obtained so far through cross correlation experiments, a conservative estimate shows that 100 nm defect generates 6 % change in the dark field signal level compared to the total integrated diffuse scatter into the dark field, when the beam footprint is $10 \mu\text{m}^2$. It has to be emphasized that this estimate of the signal strength is rather conservative by as much as a factor two. As we will see shortly, the signal to noise ratio has a rather strong effect on the dwell time. In other words, a factor of two uncertainty in the signal strength can give rise to a factor of four uncertainty in the dwell time hence in the total scanning time. Because our signal strength estimate is a conservative, our dwell time and total scan time is also a very conservative one.

⁸ This estimate is based purely on absorption of EUV radiation. When the bright field signal reduction due to the scattering of the beam out of the bright field is considered, the bright field signal strength can be much higher. A simple calculation based on a coherent illumination predicts 4 times large bright field signal for a pure pi phase defect with the same size of completely opaque defect.

4.1.3 Noise Sources.

There are several noise sources to deserve careful considerations⁹. The first noise source is the shot noise due to the finite number of photons collected by the detector and will display $1/\sqrt{T_p}$ scaling. The second noise source is the vibration-induced intensity fluctuation. The beam passes through a variety of optical elements of finite lateral dimension (the beam overfills the optical elements) as well as alignment apertures (where the beam is trimmed). Therefore, the number of photons or intensity of the beam delivered into the detector becomes a very sensitive function of position of the beam relative to the optical elements or apertures. Considering that the distance between the first horizontal deflection mirror and the pinhole chamber is 11.8 m, a small vibration of any optical elements will be problematic when one tries to pick up a signal strength on the order of 0.1 - 1 %. The amount of vibration induced noise as a function of T_p depends on the vibration spectrum because decreasing T_p is equivalent to increasing the acceptance bandwidth of the noise. In general, the mechanical vibration tends to be concentrated in low frequency regime (> 1 ms). Therefore, the vibration noise will eventually flatten out as the dwell time is decreased below a certain value. The third "noise" source is the dark field background fluctuation. This noise arises from scattering of a partially coherent radiation from rough surface. The synchrotron radiation possesses some degree of partial coherence and when it is scattered by roughness of the multilayer, the intensity distribution displays spatial dependence. As a result, the scattered light accepted by the finite size dark field detector also displays spatial dependence. This "noise" is inherent in the detection scheme and cannot be easily removed by averaging or increasing the dwell time. In other words, this noise terms does not display any dependence on the dwell time and it's contribution is going to be constant regardless of the dwell time. Instead, the magnitude of this noise contribution *will* depend on the area of the beam. We *expect* that the background fluctuation will scale as the $\sqrt{(\text{beam area})}$. We also expect that this noise only affects the dark field detection, not bright field detection, which is also supported by experimental observations so far.

4.1.4 2.4 Determination of the dwell time.

Figure 12 illustrates the relative contributions of these noise sources as a function of the dwell time per pixel, T_p , and also shows how to determine the dwell time to achieve an adequate sensitivity for a defect of certain size. The assumptions made in generating these plots are as follows:

4. The photon flux captured by the bright field detector is 5×10^8 photons per second. It is based on the bright field signal level that is measured with the current bright field detector (Hamamatsu GaP photodiode)(See endnote for details¹⁰).
5. The number of photons that is collected by the dark field detector due to the diffuse background scattering is 0.3% of that of the bright field and the efficiency of the detector is taken to be 7%.
6. 100 nm defect is assumed to generate 0.1% signal change in the bright field and 6 % change in the dark field for $10 \mu\text{m}^2$ incident beam area. Again, this assumption is considered to be conservative by as much as factor of two.
7. The roughness of the multilayer generates $\sigma = 1\%$ fluctuation in the dark field due to speckles with spot area of $10 \mu\text{m}^2$. This number might increase when the degree of coherence of the incident beam is increased.
8. The vibration levels out for dwell time below 10 msecs. It is equivalent to claiming that the vibration frequency spectrum dose not extend beyond 100 Hz. The validity of this assumption needs to be verified with experimental data.

In Figure 12, the noise level represented is 6σ , since a signal to noise ratio of 6σ is required to achieve a low enough false alarm rate. As shown in Figure 2(a) (bright field) and 2(b) (dark field), generally the amount of noise increases with decreasing dwell time. For the bright field detection, the vibration-induced noise is dominant till 100 μsec dwell time at which point the shot noise becomes dominant noise source. The vibration noise already becomes 0.24 % (6σ) even at 1 sec dwell time. Therefore, detecting 100 nm defect or equivalently detecting 0.1 % change in the bright field is practically impossible. More realistic defect detection sensitivity in the bright field is around 400 nm with the current inspection machine with dwell time of 10 ms. For the dark field, the effect of vibration is negligible compared to other noise source. In the long dwell time regime, the speckle noise will dominate. Therefore it is not advantageous to increase the dwell time beyond 100 ms in the dark field detection scheme. On the other hand, the shot noise will dominate with dwell time less than 100 ms. In the dark field detection mode, it is practical to detect 20 % change in the signal level with 10 ms time constant.

⁹ S. Jeong, SPIE. 2000

¹⁰ Currently (with 200 lines per mm grating), typical signal level detected at the end of the beam lifetime (180 mA ring current) is slightly higher than 1 nA without any upstream filter. The calibration factor of the photodiode is 1 nA for 5×10^8 photons per seconds according to Eric Gullikson's calibration chart. One should note that the efficiency of the detector is assumed to be unity.

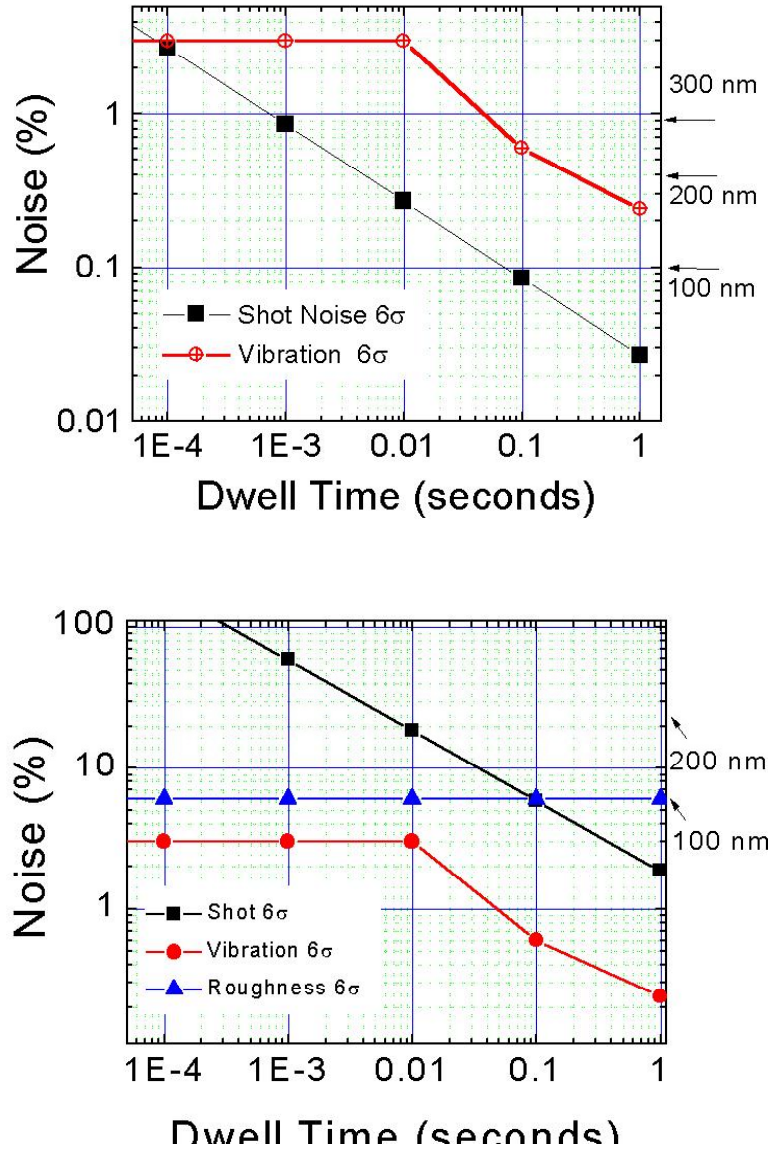


Figure 12

Noise figures for bright field and dark field detection. 6s of the each noise source is plotted in the graph and the signal levels from defects of 100, 200 and 300 nm are represented on the right.

With 10 ms time constant per pixel and pixel size of $3 \mu\text{m}^2$, the total scan time for scanning 1 cm^2 is $1\text{e}8/3 \times 0.01 = 3.3\text{e}5$ seconds = $3.3\text{e}5/3.6\text{e}3 = 90$ hours. Therefore, the current EUV inspection system can capture 20 % change in the dark field with 10 ms time constant $3 \mu\text{m}^2$ pixel size and it takes 90 hours to scan 1 cm^2 of mask blank. This is in good agreement with the recent experimental result where 1 cm^2 of mask blank was scanned in 80 hours with a dark field sensitivity of 12 % change.

For a practical scanning defect inspection system, our target scan speed is 100 cm^2 in 10 hours. It requires an improvement of 800 times improvements in scanning speed over what we have right now. The improvement is essentially coming from by focusing more photons into a smaller beam area. It is easy to show that given a focusing optical system, the total scan time is inversely proportional to the product of the photon flux and area demagnification ratio¹¹. Therefore, the

¹¹ Although this figure of merit does not have a spot size specifically, the spot size needs to be made smaller so that the signal to noise ratio is such that we are limited by the photon shot noise. For example, the figure of merit predicts that the a 10X (100 X in area demagnification) reduction optical system provides the same scanning time regardless of whether spot size is $1 \mu\text{m}$ or $10 \mu\text{m}$. When the spot size is $1 \mu\text{m}$, the object pinhole is $10 \mu\text{m}$ in size while it is $100 \mu\text{m}$ when the spot size is $10 \mu\text{m}$. This figure of merit is valid as long

improvement is sought after by increasing the photon flux and increasing the area demagnification ratio with spot size $1\mu\text{m}$.

4.2 Conceptual design for high-speed scanning

We propose to achieve the aforementioned improvements by utilizing the 20x Schwarzschild optics with modification of the current beamline. The concept for the proposed system is shown in Figure 3. The 20x Schwarzschild optics demagnifies the pinhole illuminated by the incoming EUV beam from the beamline. The object pinhole size is $20\mu\text{m}$ so that we can achieve $1\mu\text{m}$ spot size in the wafer plane. The horizontal direction of the beam propagation in the beamline is changed into a vertical direction with use of a 45 degree turning mirror with multilayer coating. To support high speed scanning with reduced noise, the sample is spun while translating slow in the other dimension so that coverage of the whole sample is achieved. We expect that the space constraint of the 20X Schwarzschild optics will necessitate the use of the turning mirror after the reflection off the sample. However a clever mechanical design might be able to dispense with it. In this proposed system, the area demagnification of the system becomes 400 compared to 30 in the current inspection system (a factor of 13 improvement in throughput). One drawback of this approach is that the photon throughput of the system is low due to the presence of several multilayer coated elements. The ratio of photons after the pinhole to that before the detector is 6.5 % assuming the 45 degree multilayer mirror reflectivity is 60 %, 20X optics has 30 % transmission, sample has 60% reflection and the final deflecting mirror has 60% reflectivity. Therefore, the photon throughput becomes 6.5 % compared to 19.2 % of the current system (a factor of three reduction in throughput).

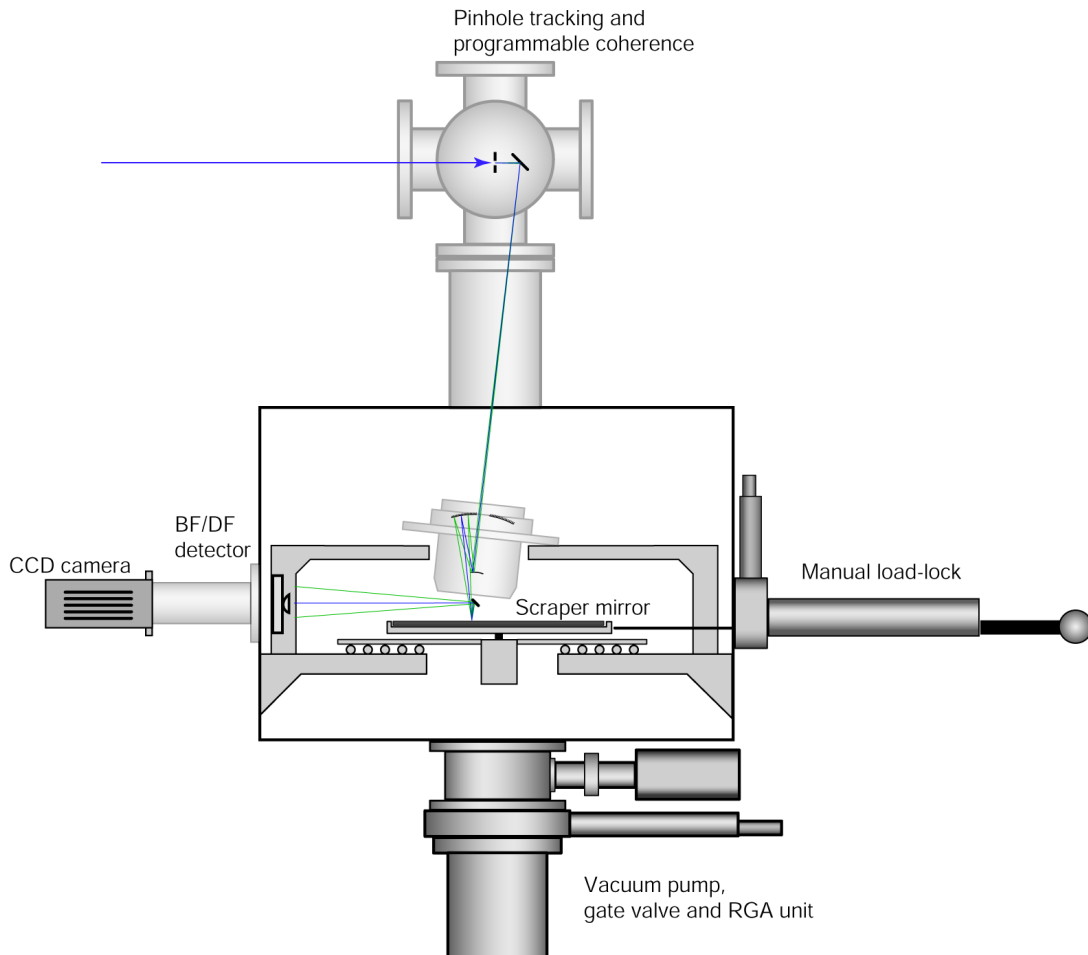


Figure 13

10x based system operating in defect scanning mode. A $1\mu\text{m}$ diameter spot is imaged scanned across the mask, with bright and dark field scattering signals simultaneously detected.

as the assumption of photon shot noise dominance is maintained. When the spot size is $10\mu\text{m}$, the expected signal from a 100 nm defect is 0.01 % change in the bright field signal which is very hard to measure without any additional electrical noise. Therefore, to maintain the system to be shot-noise limited, the signal needs to be 1% or more, which requires that the spot size needs to be $1\mu\text{m}$ or better.

4.2.1 Photon flux

The improvement in the photon flux can be classified into two categories. One is to upgrade or change the current bendmagnet beamline 11.3.2 so that we can get every last drop of the available photons. Another is to make use of the undulator beamline 12.0. In the second case of using beamline 12.0 we expect to achieve more than 1000 x increase in available EUV flux inside the bandwidth of the multilayer. This is simply because the undulator source is much brighter than the bendmagnet beamline. From this point on, the modification of the beamline 11.3.2 to achieve more flux is discussed. There are two steps to be taken to collect more photons from the current BL 11.3.2. One is to reduce the resolving power of the monochromator and the other is to optimize the spot size at the center of the pinhole chamber so that a more photon is transmitted through the pinhole.

First, let's take a look at what we can do to reduce the resolving power of the monochromator. One simple implementation is to replace the grating with the combination of a plane mirror with a multilayer coated mirror to filter the EUV radiation that's within the ML bandwidth. The bandwidth of this system becomes $1/30$ ¹². Therefore we expect to an increase of $730/30 = 24$ times in terms of available flux. This increase in flux has been confirmed experimentally (See Appendix for the details of the experiment).

The second improvement is the optimization of the beam profile at the pinhole chamber. In the current system, the spot size is 300 μm by 100 μm and the pinhole size is 25 μm . Therefore, most of the light is thrown away. If we can make the spot size smaller then we can utilize more photons for inspection. However, making the spot size arbitrarily smaller does not provide any advantage at some point. Because the reduction in spot size is accompanied by the increase in the divergence, at some point the beam divergence becomes bigger than input numerical aperture of the 20X Schwarzschild optics which is 4.4 mrad half angle. In the current beamline, the beam divergence at the center of the pinhole chamber is 1.85 mrad (full angle) in the horizontal direction and 4.4 mrad (full angle) in the vertical direction. These numbers indicate that there is a room for decreasing the spot size by a factor of 4 in the horizontal direction and a factor of 2 in the vertical direction. This improvement in the spot size is achieved by modifying the beamline. As was discussed in the previous section, the current beamline is constructed in such a way that it achieves 1:1 image of the source in the horizontal direction and 1:1 image of the exit slit in the vertical direction. An additional focusing in the vertical direction can be achieved by moving the pinhole chamber closer to the M3 (vertical focusing mirror) so that M3 is situated at 1:2 point between the pinhole chamber and the exit slit. The M3 is a bendable mirror and we can adjust the focusing of the M3 so that we can achieve tighter focusing. For the focusing in the horizontal direction, we need to insert an additional focusing mirror to achieve extra power. It is straightforward to calculate the mirror parameters to achieve extra focusing using a simple ray tracing and the findings were the mirror has to be situated m away from the pinhole and it needs to be a bendable mirror so that the spherical aberration is minimal. The ray tracing result shows that we can achieve 4x focusing at the pinhole with a right amount of bending and the depth of focus of the system is adequate (See appendix for the details). In its implementation, the extra focusing mirror can be situated inside the pinhole chamber. This extra focusing will provide us $4 \times 2 = 8$ times increase in available flux. The reflectivity loss due to the extra mirror is assumed to be 0.7.

In summary the modification of the beamline with 20X Schwarzschild focusing optics can provide $24 \times 13 \times 16 \times 0.7 \times (1/3) = 576$ times. Therefore, we expect a relative increase of 576 times compared with the current system at the same defect sensitivity when the system is installed at BL 11.3.2. When the system is installed at BL 12.0 the flux gain is more than enough to support 1000 x faster scanning rate. In this case, there is no need to modify the beamline and we can use more common 10X schwarzchild optics instead of 20x.

4.2.2 Quantitative Analysis of the throughput.

The previous throughput analyses provide a relative comparison with the current inspection system as a baseline. The advantage of the relative comparison is that we can ignore uncertainties involved with the signal strength from defects and detector efficiency. However, it is strongly desirable to list the quantitative numbers at each stage of the beamline so that one can compare this number when the real system is installed. In this section, we will list "typical" experimental measurement of the photon flux at each stage of the system assuming the system is in BL 11.3.2 operation and mirror blank with 45 degree multilayer mirror.

¹² The bandwidth of a single multilayer mirror is wider than $1/30$. However, because we are using a total of five multilayer elements, it is expected that there is a reduction in the bandwidth. $1/30$ is the bandwidth considering the reduction in the multilayer bandwidth. If there is a center wavelength mismatch between the multilayers, the bandwidth or the resultant transmission is expected to be smaller.

Currently the measurement photon flux within the bandwidth of the multilayer is $51.3 \mu\text{A} = 2.77\text{e}13$ pps (see Appendix A.1). When we consider the extra focusing optics employed, the 70 % reflectivity decreases the photon flux to $1.94\text{e}13$ pps ($= 35.9 \mu\text{A}$). The spot size at the center of the pinhole chamber is $75 \mu\text{m}$ by $50 \mu\text{m}$ with the additional focusing. Therefore the transmission through the pinhole is expected to be $(20*20)/(75*50) = 1/9.375 = 10.6 \%$.

In order to understand how to scale up the scanning speed, it is necessary to note the figure of merit for scanning speed is the photon intensity at the object pinhole times the area demagnification factor. In the current inspection system, the demagnification factor is around 50 because 25 by $25 \mu\text{m}$ pinhole is demagnified into 2.5 by $4 \mu\text{m}$ spot size. Our proposal suggests that we achieve $900 \times$ improvements in scanning speed with a combination of higher demagnification with the use of normal incidence Schwarzschild optics and increased flux. Currently two schemes are proposed. One is to modify an existing $10\times$ optics into $20\times$ so that we achieve $400 \times$ aerial demagnification (8 fold increase compared to the current demagnification factor of 50) and seek the other factor of 125 increase from the increase in flux. The second scheme is to use $10\times$ without modification so that we can get a demagnification of 100 (2 fold increase) and seek the rest $500 \times$ improvement from the incident photon flux. In either case, the resultant spot size would be $1 \mu\text{m}$ for inspection. Because the spot size is decreased from $10 \mu\text{m}^2$ to $1 \mu\text{m}^2$ (ten-fold improvement), the signal level that we seek for 100 nm increases from 0.1% to 1% (bright field) and from 6% to 60% for the dark field). The pixel size is expected to be $0.3 \mu\text{m}^2$ (with the same factor of oversampling), the total number of pixels per 100 cm^2 is $100*1\text{e}8/0.3 = 10/3 * 1\text{e}10$ pixels. To cover this many pixels in 10 hours, which is $3.6\text{e}4$ seconds, The dwell time should be $3.6*0.3\text{e}-6$ seconds $= 1 \mu\text{s}$. Assuming that in both bright field and dark field, shot noise is the dominant noise source, the required photon flux F_0 can be calculated by

$$6/\sqrt{F_0 * 1\text{e} - 6} = 0.01 \text{ for bright field and}$$

$$6/\sqrt{F_0 * 1\text{e} - 6 * 0.003 * 0.07} = 0.6 \text{ for dark field.}$$

From the bright field, it requires $F_0 = 3.6\text{e}11$ photons per second (pps) and $4.76\text{e}11$ pps for the dark field. Therefore the number of photons that needs to be detected is $4.76\text{e}11$ pps. In terms of the photodiode response, it corresponds to $3.6\text{e}11/5\text{e}8 = 952 \text{ nA}$. It corresponds to 952 times increase in flux of photons detected by the bright field detector compared to what we have in the current scanner.

The proposed system to achieve $1 \mu\text{m}$ spot size is to use Schwarzschild optics either in $10\times$ or $20\times$ configuration. In the next section, the system concept is reviewed along with the system throughput and the amount of flux that we need from the beamline is calculated. The current flux from beamline 11.3.2 and beamline 12.0 is compared against the required flux. In addition possible improvements in the system design is mentioned to optimize the incident flux in beamline 11.3.2.

The system after the object pinhole is shown in Figure 13. After passing through a pinhole placed at the object plane of the Schwarzschild optics, the beam is deflected by a 45 degree multilayer-coated mirror into the optic. The beam passes through the optic and reflected off the sample and deflected by the "scraping mirror" toward the detector assembly. The system throughput can be easily calculated. For example, 45 degree mirror introduces 40% loss (60% transmission). The throughput of the Schwarzschild system is taken to be 0.3 and the combination of sample and the scraping mirror is 0.3 . Therefore, the total system throughput is estimated to be $0.6*0.3*0.3=0.054$. Therefore, only one out of twenty-two photons are delivered into the detector¹³. Therefore, the photon flux that we need to measure before the 45 degree turning mirror is $952 \text{ nA}/0.054 = 17.6 \mu\text{A} = 8.8\text{e}12$ pps. This flux is after the object pinhole and the flux from the beamline needs to be higher by the transmission factor through the pinhole. Below we will discuss the flux available from the BL 11.3.2 (bend magnet beamline) and BL 12.0 (undulator beamline)

4.2.3 Selection of beamline

4.2.3.1 Operation on beamline 11.3.2

The beamline 11.3.2 is a bend magnet beamline and we are going to calculate the amount of flux that is available within the bandwidth of $1/30$ centered around 13.4 nm^* . The available flux at 11.3.2 with bandwidth of $1/20$ is estimated to be $77 \mu\text{A}$ through a series of measurements. Therefore, the available flux within the $1/30$ bandwidth is $51.3 \mu\text{A}$. The pinhole that we will be using for $20\times$ system is $20 \mu\text{m}$ pinhole. In the current beamline design, the transmission through $25 \mu\text{m}$ pinhole is estimated to be 1% . Therefore, when 20 mm pinhole is used, the transmission is going to be $1\%(20/25)^2 = 0.64 \%$. Therefore, the flux that we will be achieving after the pinhole is 328 nA , which is 53.6 times shy from the target. If $10\times$ system is employed, the pinhole size should be two times smaller (four times in area) than $20 \mu\text{m}$ pinhole and the

¹³ When there is a multilayer period mismatch between multilayer-coated optical elements, the throughput will suffer. To minimize the mismatch, the turning mirror can be a linearly-graded multilayer coating so that a portion of the coating can match the bandwidth of the rest of the system.

* The choice of bandwidth $1/30$ accounts for the bandwidth narrowing when the multiple multilayer is used. The bandwidth of a single multilayer is $1/20$.

transmission through the pinhole decreases by four times, resulting in the available flux of 82 nA. This number is 215 times smaller than what we needed.

There are several improvements to be made to bring this number closer to the target. First, the 4-jaw aperture can be opened up and provide 70 % more flux. The measurement of the inband flux due to the whitelight was performed with four-jaw aperture closed by half. The four-jaw aperture was closed to remove the tail in the KB focused spot. If we open the four-jaw aperture, we see an increase of 1.79 times with monochromator tuned at 130 Å. Therefore, when the four jaw aperture is fully open we expect to achieve 1.7 times flux increase.

The second improvement we can make is to bypass the scraping mirror for bright field detection. The bright field detector, photodiode, is rather compact. Therefore we can drill a hole at the scraping mirror and reflect the dark field into the dark field detector while the bright field signal is accepted by the photodiode. This will provide additional 1.6 times improvement.

The third and biggest improvement to be made is to match the beam divergence to the input N.A. of the Schwarzschild optic by tight focusing of the beam in the beamline with substantial increase in pinhole transmittance. The Schwarzschild optic has an input N.A. of $0.088/20 = 4.4$ mrad when the system is configured for 20x. The full divergence of the BL 11.3.2 at the pinhole plane is 4.4 mrad in the vertical direction and 1.85 mrad in the horizontal direction with beam profile of 300µm (horizontal) by 100µm (vertical). Therefore the smallest spot size we can achieve while we match N.A. of the Schwarzschild optic is 75µm by 50µm, improving the transmission through 20µm pinhole by as much as 8 times. These N.A. matching or tight focusing can be achieved by (1) placing the pinhole closer to the vertical focusing mirror so that we can achieve 2:1 demagnification between the exit slit and the pinhole and (2) placing additional optics to aid in horizontal focusing. Through a ray-tracing simulation using SHADOW, it was shown that an extra horizontal focusing mirror can be designed and can achieve a tighter focusing. The extra mirror (glancing angle optics) introduces loss of photons about 0.8. When these three improvements combined, we expect to achieve $8 \times 1.7 \times 1.6 \times 0.8 = 17.4$ times flux gain. Therefore, we can scan 100 cm² in 31 hours with optimization of flux in beamline 11.3.2.

4.2.3.2 Operation on beamline 12.0

BL 12.0 is an undulator beamline with a high brightness. The undulator beamline is expected to support 16µA through a pinhole as small as 10µm even with the monochromator. For example, currently at the entrance pupil of the 10 x camera, EUV power of 33µW is measured when the upstream pinhole size is 0.75µm. Applying the conversion factor of 0.13 A/W it corresponds to 4.2µA. The size of the beam in front of the pinhole is 4x8µm. Therefore, if the pinhole is taken out, the flux becomes about 200µA, which is about 10 times higher than what we need. Therefore, with BL12.0 operation, the photon flux has a factor of 10 leeway. The divergence angle of the beam is 9.6 mrad (full angle) which is smaller than the input N.A. of 8.8 mrad (half angle).

In summary, when the system is installed at BL 11.3.2, the scanning speed is 31 hours for 100 cm² with optimization of the beamline along with employment of 20x optics. In contrast, in the BL12.0 operation, the beamline has enough flux to support scanning rate up to 1 hours per 100 cm² and the scanning rate is only limited by the data acquisition system and its supporting architecture. Furthermore with BL 12.0 operation, there is no need to modify the existing 10x into 20x, which results in savings in cost and time. Because BL 12.0 is a very heavily subscribed beamline, one approach is to use BL 11.3.2 for system integration/development and testing. Once the system operation is in mature state, the system can be moved to BL 12.0 and can be operated for real high speed operation. This hybrid approach can save time and money and minimizes the disruption in the BL 12.0 operation because this approach does not involve any modification to the 10x optics and no beamline modification.

However, as previously discussed time on beamline 12.0 is heavily booked and space is at a premium. Therefore we are going to stay on beamline 11.3.2 and extend the capacity of that system as far as possible for the purposes of this project. Given the nature of the correlation experiments likely to be performed a scan time of 31 hours for 100 cm² is not unreasonable for a system that is not intended to perform production-scale mask blank inspection.

4.3 **Key subsystems**

4.3.1 10x camera

A 10x Schwarzschild camera modified to operate at 20x magnification is used to image a pinhole into the mask at 20x reduction. This camera has demonstrated diffraction limited performance to 100nm at 0.08NA facing the mask. The chief ray angle of incidence of the 10x camera is 12.5°, so the camera is tilted at 6.5° to make the angle of incidence equivalent to the 6° angle of incidence anticipated for a production stepper system¹⁴. This ensures that shadowing effects and wavelength are properly matched to a production mask set. When modified to operate at 20x magnification the track length of the Schwarzschild objective is 570mm, which is not an unreasonable path length given for this type of system.

¹⁴ Tilting the camera reduces the useable field of view if the camera is used for full-field imaging as discussed in the LLNL Aerial Image Microscope design study of 2002. However when used as the projection lens in a scanning system the corrected field of view with 6° tilt is adequate to support the 1µm diameter illuminated spot size required for defect scanning mode.

4.3.2 45° fold mirror

The fold mirror is required and is in fact desirable for several reasons:

1. In the proposed concept design the mask is located in the horizontal plane, thus a fold mirror is required in order to turn the horizontal beam from the ALS into the camera;
2. If the beamline is run in white light mode to maximise flux the fold mirror is the first bandwidth-limiting optic and therefore takes the full source bandwidth. It is desirable to have this as an easily replaceable mirror rather than, say, the primary optic of the camera where replacement would be costly and time consuming in the event of contamination or damage;
3. The two multilayer-coated optics in the Schwarzschild camera, combined with the 45° fold mirror, provide three multilayer reflections for wavelength and bandwidth selection. If the beamline is run in white light mode these three reflections are what defines the wavelength and bandwidth incident on the mask.
4. When run in imaging mode, having a moveable mirror enables the use of programmable coherence, giving greater control over the partial coherence used in imaging mode. It also allows some degree of beam steering into the camera, giving greater control over system alignment.

Note that the light from the bend magnet source is polarised in the horizontal plane, thus the efficiency of the 45° mirror will be 75% or better, minimising the throughput hit incurred through its use.

4.3.3 Pinhole tracking

Due to a slow beam drift in the beamline, the overlap between the object pinhole and beam changes with time. This is an effect separate from high frequency vibration. The mismatch between the pinhole and the beam makes the vibration problem more visible due to the increased beam slope. To mitigate this problem, two approaches can be utilized. One is to actively control the mirrors so that the overlap between the beam and pinhole is actively controlled to maintain its optimum position. This approach has the drawback that the whole mirror tank needs to be adjusted because the mirrors are attached to the mirror tank in the current beamline design. The second approach is to make the pinhole track the beam position. This is easier to implement than the first method. Due to the pinhole movement in the object plane, the image of the beam will also move. However, considering that the typical slow drift in the beam position is less than 100 µm in the pinhole plane, the image movement becomes less than 10 µm (in 10x reduction) or 5 µm (at 20 x reduction) which is much smaller than the registration error budget due to the mechanical housing.

Experience with the existing defect inspection beamline indicates that there is significant (up to a few hundreds of microns, but typically less) drift in the position of the beam over time due to thermal effects in the beamline. This drift in turn leads to variations in flux passing through the pinhole that give rise to a varying background signal level, effectively introducing an additional noise source into the detection system. In order to minimise the effect of these fluctuations on measured signal a strategy of pinhole tracking is employed to ensure that the beam remains centered on the pinhole. Employing this strategy has two advantages:

1. The pinhole is kept at the brightest part of the beam, maximising flux through the pinhole; and
2. The intensity gradient with regard to x-y position at the brightest part of the beam is zero, thus small movements in beam position caused by acoustic vibration lead to the minimum possible variation in transmitted flux.

We propose to retain the already implemented beam tracking system in the upgraded design; it can always be turned off if not required.

4.3.4 Brightfield/Darkfield detector

A dual-channel brightfield/darkfield detector is incorporated to allow simultaneous detection of these two data channels. In the current scanning system greatest sensitivity to buried defects has been observed in the darkfield channel, however it was also observed that some defects manifested themselves primarily in the brightfield channel with little associated darkfield scattering. Simultaneous data collection is therefore desirable to capture all types of defects. A dual-channel detector similar to the current system will be employed. A photodiode will be used for brightfield detection, and either an avalanche photodiode or multichannel plate will be used to capture the darkfield signal.

4.3.5 Scraper mirror

Space underneath the camera housing is limited to approximately 25mm and there is limited scope for recessing detectors inside the camera housing, making it difficult to fit the detectors within this space. The only practical way in which to have detectors within this space would be to mount a custom segmented photodiode beneath the camera with a hole drilled in it to pass the illuminating beam. We are exploring this as an option, but if no adequate solution is found at reasonable cost for direct detection it is likely that a scraper mirror will be required to redirect the specular and scattered light into the horizontal direction towards detectors located on the chamber wall away from the mask. Due to the polarised nature of the synchrotron beam a scraper mirror is expected to incur only a 70% throughput hit.

4.3.6 Scanning stages

An upgrade to the existing stages will be required in order to support high-speed mask scanning. If an x-y raster scan is employed there is typically a factor of 3 dead-time due to direction changes at the end of each scan line. This represents a direct throughput hit as no scanning is performed during the stage turnaround time. A better option is to rotate the mask under the scanning spot as this ensures continuous data collection, in which case a combined rotation-translation stage with encoder readout is required. It is also possible to get a rotational scan pattern from x-y stages by driving the x and y axes independently with out of phase sine waves. Whilst the motion is not as elegant as employing a rotary bearing, the use of x-y encoders simplifies the task of registering defect locations. It may also be easier to design and buy a reliable x-y stage with the required precision than a custom rotation/translation stage.

Projected scanning mode performance is important for high-resolution operation. The projected scanning speed can be limited by either available photon flux required to achieve a given noise level, or by hardware limitations such as stage speed or data acquisition rate.

The current data acquisition hardware on BL11.3.2 uses a VXI crate connected to a Sun workstation over a VME bus, an architecture that can support 100-500kHz (2-10 μ s/sample) data acquisition rates relatively easily. Moving to significantly faster data acquisition rates requires the use of dedicated DSP processing, which is possible but adds complexity to the system design. If we peg the system data acquisition speed conservatively at 100kHz with a 1 μ m spot size in inspection mode, the linear scan speed is $(1 \times 10^5 \text{ points/sec}) \times (1 \mu\text{m/point}) = 1 \times 10^5 \mu\text{m/sec}$ or 10cm/sec linear scan speed. There are 10^8 square microns of area in a square cm, thus the theoretical maximum scan speed with a 1 μ m spot at 100kHz is 3.6cm²/hr. This calculation is summarised in Table 2 below.

Data acquisition rate	100 kHz or better (up to 1MHz)
Measurement spot size	1 μ m
Linear scan speed	10 cm/sec
Area scan rate with zero latency	3.6 cm ² /hr
Peak scan speed achieved with current system	5 hr/cm ²

Table 2

Selection of scanning pattern can have a significant effect on scan speed. For example, employing an X-Y raster scan typically involves an increase in scan time by a factor of three due to the requirements to turn around the mask at the end of each scan line. If possible it would be good to avoid such a loss in throughput by rotating the mask to maintain a continuously high scan rate by avoiding turnaround delays, and to maintain a constant data rate it is desirable to increase the rotation speed as the scan spot moves closer to the axis of rotation. Maintaining a 10cm/sec linear scan speed at the edge of the mask requires the mask to be rotated at 0.2rev/sec (5sec per revolution), which can be increased as the scan spot moves towards the centre of the mask as shown in Figure 14, where the rotation speed has been capped at 1rev/sec near the centre of the mask where high rotation speeds would otherwise be required. Applying this scan pattern it is possible to scan 176cm² of mask in under 52 hours (2.2 days) of inspection time with an average scan speed of 3.4cm²/hr, which is close to the maximum scan speed possible at the target digitisation rate.

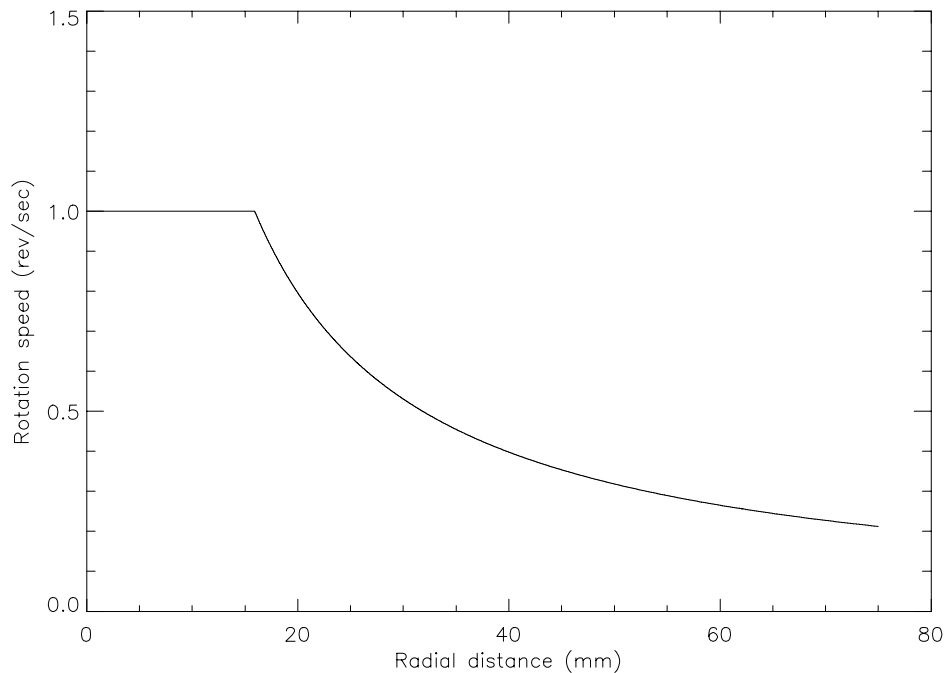


Figure 14

Rotation speed of the mask required to maintain the desired scan speed as the spot is moved radially inwards. (The rotation speed has been capped at 1rev/sec near the centre of the mask.)

4.3.7 Vibration control

With a spot size on the mask of $1\mu\text{m}$ diameter it will be necessary for system vibrations to be controlled to better than this value so as to ensure that the entire mask surface is uniformly scanned. Floating the vacuum chamber on vibration isolation supports is impractical as alignment must be maintained with the ALS beam, which is fixed in space relative to the floor. However placing the entire apparatus on an optical table should dampen vibrations significantly. The x-ray microscope XM-1 is built on an optical table bolted to the floor with kinematic mounts and routinely obtains 25nm or better resolution with second-long exposure times.

4.3.8 Cleanliness: particle

The number of particles added during sample handling and scanning needs to be below 0.1 per cm^2 for the proposed system*. This requirement is dictated by the level of defect that we are trying to count and compare. We envision that the sample will be scanned in the optical scanner and EUV scanner repeatedly for comparison. For example, if it is suspected that some particular defects dropped during the transport, it has to be rescanned for checking. Therefore, we need to keep the level of adders low enough so that repeated scan does not hamper map-to-map comparison.

4.3.9 Load lock

Clean handling requires slow pumping and venting protocols to be employed. A load-lock is therefore desirable to minimise the amount of time spent pumping and venting the large main chamber when changing samples. Experience at LLNL indicates that added defect densities of the order of $0.01/\text{cm}^2$ are achievable using careful manual loading and proper pump/vent protocols therefore a manual load-lock is likely to be adequate for this system. However, the load-lock interface will be designed with possible upgrade path to robotic SMIF mask handling should the need arise.

4.3.10 Cleanliness: organic contaminant

The system has to be clean enough so that the optics and sample can remain damage-free after extended radiation exposure. We need to have hydrocarbon-free environment where the Schwarzschild optic and sample is located. The region where 45 degree folding mirror and pinhole is situated might have to be isolated from the main chamber. So that the vacuum condition is much better in the sample chamber so that multilayer mirror coating in the Schwarzschild optics is not damaged after long extended radiation exposure.

* This added defect density requirement is weaker than what is required for a system qualifying production mask blank. If a system is to be used for final qualification step it should add zero defect.

4.3.11 Depth of focus control

We need a capability for depth of focus control to have the sample focused on the sample. The spot size can be monitored monitoring the auto-correlation of the dark field speckle pattern or using an independent focus monitoring sensor. This monitoring technique can be used to translate the optic so that the sample is within the depth of focus of the inspection system. Alternatively precision capacitance gauges can be used to monitor the separation between the camera and the mask, providing feedback for keeping the mask in focus. The sample stage should not have significant tilt so that sample moves out of focus.

4.3.12 Vibration compensation using signal processing.

In the bright field, the vibration is going to be the dominant noise source if not compensated. One advantage of fast scanning is that the data acquisition rate is in the realm of MHz or several hundred kHz where the mechanical vibration power density is expected to be virtually none. Therefore, we can use high-pass filtering to compensate relatively low-frequency vibration. For example, if there is an isolated defect, its signature will appear only three pixels (3x oversampling) which corresponds to 3 μ sec with 1 μ sec dwell time per pixel. This is a very high bandwidth signal. If we perform a high pass filtering with cutoff frequency with 10 kHz, the signal strength reduction or distortion to the signal from an isolated defect will be minimal, while the noise source below 10 kHz (mainly mechanical vibration) will be significantly suppressed. Whether this type of signal processing occurs on the fly (in real-time) or off-line depends on the data acquisition architecture.

4.3.13 Flare of the focusing optics:

The Schwarzschild optic that we are going to be employed in the system usually possesses a very high level of flare. The flare becomes a problem in reducing the signal contrast. If a significant amount of flare is captured by a dark field detector, the contrast is reduced dramatically due to the high sensitivity of the dark field detector. The flare of the optics needs to be minimized and the dark field detector angle needs to be opened up not to capture any flare component.

4.3.14 The need to retain the 20X interferometer

If we use a 20x camera, it's possible that the 20x mirror system might go out of alignment. Therefore, someone might argue that the interferometer for 20x alignment needs to be maintained instead of being disposed after the initial alignment. This is rather a business decision than a technical decision.

4.4 Conceptual design for high-resolution imaging

A modification of the above system for operation in high-resolution mode as a zone plate microscope is detailed below:

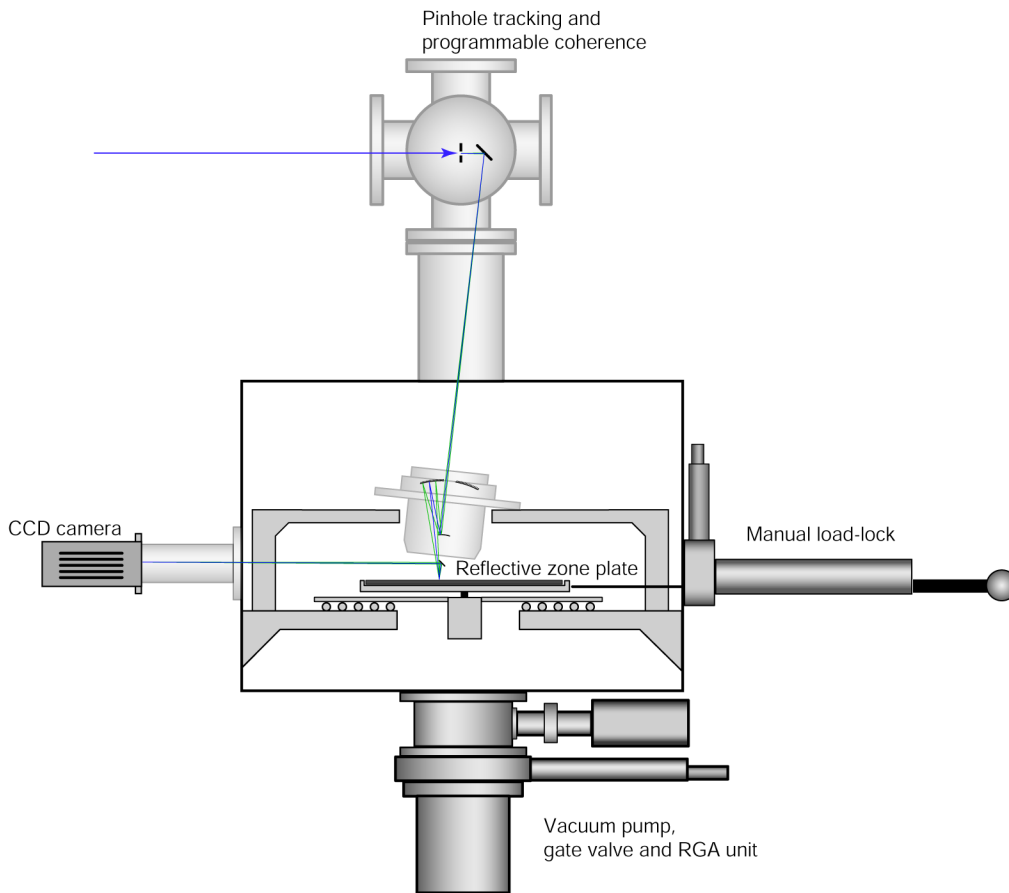


Figure 15

Defect inspection system modified for operation in high-resolution imaging mode. The scraper mirror is replaced with a reflective zone plate lens, with an image of the mask being formed on an EUV CCD camera located to the side of the chamber.

4.4.1 Zone plate lens design

Most zone plate microscopes, for example XM-1, operate in transmission mode, in which case the condenser and imaging optics are on opposite sides of the object and do not interfere with each other. With a reflective EUV mask it is necessary to fold the system back on itself so that both the illumination and imaging optics are on the same side of the object. Furthermore, for the system considered here there is limited space beneath the camera housing (25mm clearance from the housing to the mask), making it impractical to construct a complete zone plate microscope underneath the optic itself, whilst the physical dimensions of the housing preclude letting the image-forming rays pass through the camera itself. The easiest way in which to maintain a zone plate imaging capability within the system design is to incorporate a 45° turning mirror into the system so that an image is formed off to the side of the mask. This can be done in one of two ways: either a conventional, circular zone plate can be suspended beneath a plane fold mirror, or a modified the zone plate can be patterned directly onto the turning mirror.

The simplest zone plate design contemplates a single imaging element (zone plate) imaging the mask with a 0.0625NA zone plate tilted with respect to the mask so that the optical axis of the imaging system is at 6° to the mask. The imaging system is therefore a tilted optical system and as such will suffer from keystone distortion and require a tilted

image plane¹⁵. It is possible to correct for this by using an off-axis portion of an on-axis zone plate to eliminate keystone distortion and to have the object and image planes parallel to one another and the zone plate, as shown in Figure 16 below:

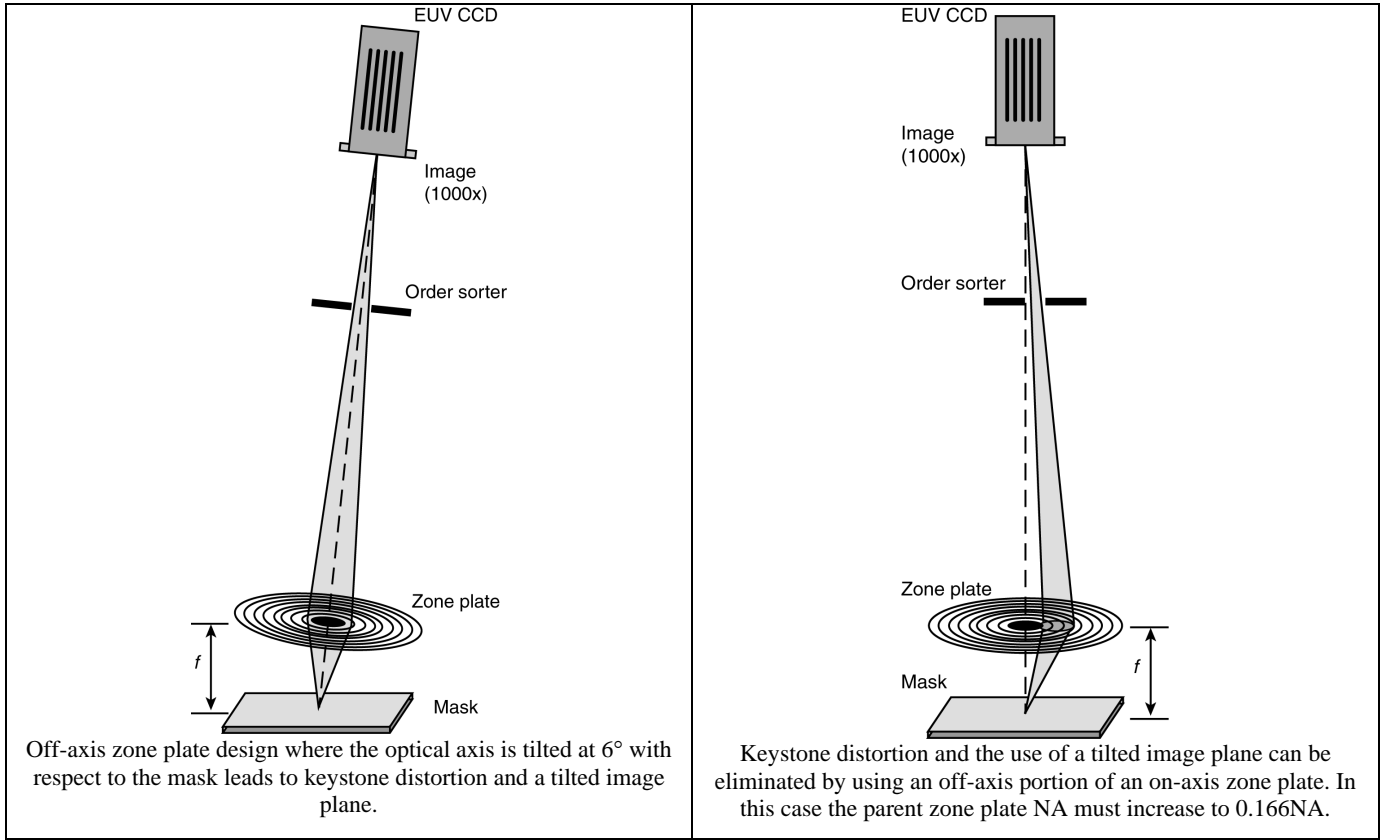


Figure 16
Off-axis and on-axis zone plate designs.

This on-axis zone plate design has the advantage that the zero and first order diffraction orders are physically separated, reducing flare in the system and allowing for more relaxed placement of the order sorting aperture. In order to capture the marginal ray of the 0.0625NA AIM pupil at 6° angle of incidence using the on-axis design illustrated in Figure 16 it is necessary to have a parent zone plate with a numerical aperture of 0.166NA. This is the design we choose to analyse in detail below.

4.4.1.1 Relationship between bandwidth, focal length and working distance

As described in the down-selection report a zone plate is completely specified by the wavelength, bandwidth and resolution. In particular we have the following relationships:

Outer zone width: $\delta = \Delta r_N = \lambda / 2NA$

Number of zones: $N < \lambda / \Delta \lambda$

Focal length: $f = 4N\Delta r_N^2 / \lambda$

Diameter: $D = 4N\Delta r_N$

Field of view: $FOV \approx D/3$

We therefore see that, unlike multilayer coated optics, the desired bandwidth, which sets the number of allowed zones N , plays a major role in determining the design of a zone plate system. For an AIM system we require a 0.0625NA pupil giving a zone spacing $\Delta r_n = 107nm$ for all system. The wavelength is fixed at 13.5nm, thus the only undetermined parameter is the bandwidth. For a 6-mirror camera plus mask and condenser optics the bandwidth is anticipated to be 2%, however for practical reasons a vendor may choose to operate at a different bandwidth.

¹⁵ The effect of tilting an objective on keystone distortion, image plane tilt and through-focus behaviour was discussed in the section on tilted Schwarzschild concepts, and much of this discussion is also relevant to a tilted zone plate system.

For the on-axis design, the width of the outermost zone is 40nm and we have:

2% bandwidth = 6 mirror camera + mask and condenser optics	
Parent NA:	$NA = 0.166$
Outer zone width:	$\Delta r_n = 40nm$
Number of zones:	$N = 50$
Focal length	$f = 24\mu m$
Diameter:	$D = 8\mu m$
Useable field:	$FOV = 2.6\mu m$
Working distance from zone plate to mask:	$24\mu m$
0.1% bandwidth = LBL subfield exposure station	
Parent NA:	$NA = 0.166$
Outer zone width:	$\Delta r_n = 40nm$
Number of zones:	$N = 1000$
Focal length	$f = 477\mu m$
Diameter:	$D = 160\mu m$
Useable field:	$FOV = 53\mu m$
Working distance from zone plate to mask:	$0.47mm$
Track length:	$0.5m$ for 1000x magnification

Table 3

Design parameters for an on-axis zone plate design, parent NA=0.166.

Inspection of the above table shows that, for an on-axis design, capturing the full 2% bandwidth of a stepper system leads to a very small working distance of $24\mu m$ between the mask and zone plate not including any additional clearance required for mounting hardware. This places the zone plate very close to the mask and requires demonstrating an accurate and reliable positioning system to avoid accidental contact with the mask. A more practical working distance of 0.5mm, which allows greater margin for error and is within the target range of 0.5-1mm working distance, can be achieved by restricting the bandwidth to of the order of 0.1%, as shown in the above table. This entails a significant departure from the bandwidth of a production stepper system, thus the effect of reducing the bandwidth on the equivalence between the measured AIM image and the result obtained in a stepper need to be carefully evaluated to ensure that no artefacts are inadvertently introduced through using narrower bandwidth illumination. The effect of bandwidth restriction on source requirements and condenser design must also be considered as it is necessary to design a condenser capable of providing the reduced bandwidth which, depending on source spectral properties, may in turn require discarding EUV photons from the source, thereby increasing the overall drive power required.

For the sake of completeness we also provide calculations for the on-axis design by way of comparison:

2% bandwidth = 6 mirror camera + mask and condenser optics	
Parent NA:	$NA = 0.0625$
Number of zones:	$N = 50$
Focal length	$f = 170\mu m$
Diameter:	$D = 21\mu m$
Useable field:	$FOV = 7\mu m$
Working distance from zone plate to mask:	$170\mu m$
Track length:	$0.17m$ for 1000x magnification
0.1% bandwidth = LBL subfield exposure station	
Parent NA:	$NA = 0.0625$
Number of zones:	$N = 1000$
Focal length	$f = 3.4mm$
Diameter:	$D = 0.43mm$
Useable field:	$FOV = 140\mu m$
Working distance from zone plate to mask:	$3.4mm$
Track length:	$3.4m$ for 1000x magnification

Table 4

Design parameters for an off-axis zone plate design. Due to the reduced parent NA the focal lengths and bandwidth requirements of this system are different to that required for an on-axis design.

From this table it is apparent that a system that captures the full 2% bandwidth has a very small focal length ($170\mu\text{m}$), which means that the working distance from the zone plate to the mask would be of the order of $170\mu\text{m}$ not counting any mounting hardware. The only practical way to increase the focal length and, hence, the working distance to the mask is to decrease the bandwidth as illustrated above. If this is done it is necessary to show through aerial image simulation and electromagnetic analysis of the mask/EUV interactions that using a reduced bandwidth will lead to the same conclusions about printability as would be arrived at in an actual a stepper system.

4.4.2 Imaging optic used as a condenser

With the zone plate performing the role of imaging optic, the camera is used solely to illuminate the mask. This is done by removing the pinhole so that an illuminated area of approximately $50\times 50\mu\text{m}$ is formed on the mask. The camera is already configured so that the angle of incidence at the mask is 6° as required for stepper emulation imaging. The clear aperture of the camera is 0.8NA, thus there is ample aperture available for synthesis of pupil fills up to $\sigma=1.0$. A scanning mirror system similar to that employed on the SES exposure station will be used in order to control coherence effects.

4.4.3 Alternative approach: scanning

The role of fast scanner is not limited to actinic mask blank defect detection. With achievement of smallest spot size ($0.2\mu\text{m}$ Airy disc) in combination with signal processing technique, the scanner can be configured to serve actinic inspection of patterned mask. In this mode, due to the small spot size, the scanning will be limited to a small area of a patterned mask. It is challenging to execute a stage stepping motion with precision of $0.1\mu\text{m}$, reliably in both directions. One method to deal with this problem is to scan the object pinhole instead of scanning the sample itself. If the object pinhole is moved $1\mu\text{m}$ ($2\mu\text{m}$), the image will move $0.1\mu\text{m}$ in 10x (20x) reduction. Therefore, the placement of the beam can be very precisely controlled. Because the beam spot has a spatial profile contained within a limited spatial extent less than $300\mu\text{m}$, the scanning area is restricted if the object pinhole is scanned in a transverse direction to the beam. However, if the object pinhole is scanned in a longitudinal direction together with 45 degree turning mirror (the object pinhole is placed after the 45 degree turning mirror), the scanning range is only limited by the depth of the focus of the beamline optics, which easily exceeds 5 mm. The scanning in the second direction does not have to be a stepping motion. For example, it can be a constant velocity scan with an accurate position sensor, just as in the current scanner. Another possible engineering solution is the beam steering using upstream multilayer mirror pairs as in optical scanner. Two multilayer coated mirror can be used to steer the beam with very high precision within the field of view of the system. Because in the pattern inspection mode, the throughput is not the primary concern, the loss due to the insertion of two multilayer coated mirrors is not a major concern.

Another possibility for high-resolution imaging of defects on mask blanks is to use holographic imaging reconstruction, where one can reconstruction the amplitude and phase of the wavefront reflected from the mask blank. This method has already been demonstrated in a separate proof-of-principle experiment and its implementation is fully compatible with the proposed system and it is only a matter of a simple design of grating order sorter aperture to pass only two orders of the beam from the grating placed in the object side of the Schwarzschild optics. With implementation of at-wavelength metrology capability, the proposed tool will become a true integrated solution to the defect inspection and characterization need for EUV lithography mask blank defects. For example, once a fast inspection captures defects on the mask blank, we can use the at-wavelength metrology capability to characterize the defects and provides the feedback on impact of the found defects on printability with aerial image simulation.

We anticipate that the system we propose to design will have sufficient flexibility to enable exploration of both of these strategies for high-resolution imaging in addition to the zone plate approach.

4.5 *Preliminary subsystem specifications*

Subsystem	Specification	Reason
Primary optic	Modified Sandia 10x camera	
	Tinsley B optic set	Set of substrates available from SNL, uncoated
	$\lambda=13.5\text{nm}$ at 6° AOI	To match MET masks
	20x magnification	Flexible – but 20x enables use of a larger pinhole
	573mm track length	Track required to get 20x magnification
	$50\mu\text{m}$ corrected field at mask	Relaxes pinhole positioning accuracy to 1mm

Subsystem	Specification	Reason
		$\pm 50\mu\text{m}$ is within the $400\mu\text{m}$ field of view of the 10x camera
	6° tilt (from vertical)	Angle of incidence at the mask should be 6° to match shadowing of production stepper. (Chief ray angle of incidence of the 10x is 12.5° , so we need a 6° tilt to get the angle of incidence to be $\approx 6^\circ$) The MET angle of incidence is 4° , which is a tight squeeze for the scraper mirror, therefore we relax to 6° .
	Kinematic mount	Metrology tower or inbuilt beam sight for alignment
Pinhole system	Re-use existing?	Will require overhaul of software, but the hardware already exists so it makes sense to re-use it.
Coherence control	Re-use design from SES exposure station	Mechanical drawings exist, compatibility with existing software drivers
Scanning detectors		
Brightfield	100kHz or faster bandwidth (up to 1MHz desirable)	Required to keep up with target scan speed
	12-bit or better digitisation	Need dynamic range for high-quality image acquisition.
Darkfield	100kHz or faster bandwidth (up to 1MHz desirable)	Required to keep up with target scan speed
	High signal sensitivity	Low signal expected in darkfield channel, although experience suggests we will operate in current mode rather than photon counting mode.
CCD detector	Eg: PI-SX as on XM-1	Compatible with XM-1 software and know-how
(imaging mode)	Back-thinned EEV42-40 CCD chip	Direct detection
	2048x2048 or more pixels	(1024x1024 would be adequate)
	$13\mu\text{m}$ pixel size	Small pixel size = lower magnification
	12-bit data depth	Required for photometric aerial image measurement
	6" conflat flange interface	Standard interface to bellows mount
Translation stages		
Rotation (θ)	0.2 to 1 rev/second speed	At 100mm/sec, 3" from mask centre, this is the range of rotational speeds
	Vertical wobble $<10\mu\text{m}$	Geometrical depth of focus of 10x system
	Horizontal wobble $<1\mu\text{m}$	Track pitch of circular scan. We may be able to relax this if it's a repeatable rather than random motion
	Interpolated encoder accuracy to $<10\mu\text{m}$ (at outermost radius)	Interpolation between points assuming constant speed is OK.
Linear (x)	$<1\mu\text{m}$ drive precision	Track pitch of circular scan.
	Position stable to $<1\mu\text{m}$	Track pitch of circular scan.
	Encoder accuracy $<1\mu\text{m}$	Track pitch of circular scan.
	$>75\text{mm}$ range of travel	Radius of circular region on 6" mask to be scanned
	$12\mu\text{m}/\text{min}$ linear speed	
Focus (z)	$1\mu\text{m}$ step size	For through-focus data sets in imaging mode.
	Encoder readout $<1\mu\text{m}$	For through-focus data sets in imaging mode. Use cap sensors on 10x housing to directly measure the absolute distance from optic? Use these for feedback?
	10mm range of travel?	For loading 2mm thick wafers and $1/4$ " thick masks ??
Mask handling		

Subsystem	Specification	Reason
Handling cleanliness	<1 particle/cm ² handling adders	Too many 'adders' and cross-registration is hard. Need
	Class 100 cleanroom adequate	Manual loading in class100 cleanrooms at LLNL has shown added defect densities of <0.05/cm ² (source: Chris Walton, Stefan Hau-Riege, Cindy Larson)
Load lock	Use SEM style load-lock	Available as OEM component
	Slow pump and vent	Particle control requirement
Main chamber		
Construction	Aluminium or SS	TBD. Aluminium requires special flanges... but is cheaper and lighter.
	Conflat or O-ring seals adequate	O-ring seals are probably adequate. Conflat flanges (rubber or metal seal) on main interface ports required for compatibility with beamline and existing vacuum pumps.
Vacuum pumps	Re-use existing turbo and gate valve?	Pat Kearney suggests keeping the turbo. Steady high-frequency turbo vibration is better than the 'knocking' motion of a cryo pump for particle control. No experience with particle level from ion pumps. Existing system has 33000hrs on the clock – how long will it last? Do we want to upgrade to MagLev bearings to help with vibration control?
Vacuum pressure	10 ⁻⁶ Torr adequate	Long absorption length at 13.5nm is main requirement
	Hydrocarbon level	Must be kept low to prevent Carbon build-up on optics. Get hard figures from Sasa, Henry or Lennie.
RGA	Retain	Make sure we test and include the existing RGA for monitoring hydrocarbon levels.
Vibration isolation	Optical table	Vibrations were a problem for the old design – adding an optical table will help damp these out.
	Use LBNL standard mounts	Compatibility and alignment stability

5 Useful additional information

5.1 Photon Flux measurement at BL 11.3.2

In this section, experimental results measuring the available flux from beamline 11.3.2 are described. The experimental procedure is described along with data and the available total multilayer inband flux within bandwidth of 1/30 centered around 13.4 nm is estimated. We measured the reading of the photodiodes at three different locations with three different combination of beamline filters and three different combination of illuminations.

The location of the photodiodes are:

PD1: After the 25 μ m pinhole in the pinhole chamber

PD3: Right before the sample inside the scanner

PD4: After reflection off the sample.

The three filters are empty, Be filter, Si filter. The filters are used to block the out-of-band radiation such as higher order and ultraviolet and visible radiation.

The three illumination conditions are: monochromator 132 Å (peak), zero order monochromator and mirror blank.

The sample that was used for this experiment had 62% reflectivity at 13.4 nm.

There were two runs of experiment to check the consistency. The experimental result is shown in the following. (See experimental book Vol 2 1/28/99)

PD1 1st Run

	mono	zero	blank	mono	zero	blank
empty	15	7000		16.5	7200	
Si		1000		4	1100	
Be		430	3800	2	440	

PD1 2nd Run

PD3 1st Run

	mono	zero	blank	mono	zero	blank
empty	5.3	2300	20000	6.2	2500	
Si	1.2	340	1200	1.3	370	
Be	0.5	150	600	0.59	160	

PD3 2nd Run

PD4 1st Run

	mono	zero	blank	mono	zero	blank
empty	1.6	46	170	1.85	66	
Si	0.57	16.5	60	0.76	22	
Be	0.23	6.5	26	0.31	9.1	

PD4 2nd Run

A.1 Summary of Experimental Results.

A.2 Analysis

(1) Throughput of the KB system.

From the ratio between PD1(empty-mono) and PD3 (empty-mono), the throughput of the KB system is estimated to be 34 % at the time of experiment*.

(2) The attenuation of the Filters.

The attenuation of in-band radiation due to the Si filter is

$$\begin{aligned} \text{PD4(empty-mono)/PD4(Si-mono)} &= 1.6/0.57 = 2.81 \quad (\text{in the 1st run}) \\ &= 1.85/0.76 = 2.43 \quad (\text{in the 2nd run}) \end{aligned}$$

The attenuation of the in-band radiation due to Be filter :

$$\begin{aligned} \text{PD4(empty-mono)/PD4(Be-mono)} &= 1.6/0.23 = 6.96 \quad (\text{in the 1st run}) \\ &= 1.85/0.31 = 5.97 \quad (\text{in the 2nd run}) \end{aligned}$$

Therefore, the attenuation factor is 2.6 for Si and 6.5 for Be for the radiation in the multilayer bandwidth.

(3) Flux increase

The increase in the in-band radiation due to the monochromator zero-order:

$$\begin{aligned} \text{PD4(Be-zero)/PD4(Be-mono)} &= 6.5/0.23 = 28.26 \quad (1\text{st run}) \\ &= 9.1/0.31 = 29.35 \quad (2\text{nd run}) \\ \text{PD4(Si-zero)/PD4(Si-mono)} &= 16.5/0.57 = 28.95 \quad (1\text{st run}) \\ &= 22/0.76 = 28.95 \quad (2\text{nd run}) \\ \text{PD4(empty-zero)/PD4(empty-mono)} &= 46/1.6 = 28.75 \quad (1\text{st run}) \\ &= 66/1.85 = 25.67 \quad (2\text{nd run}) \end{aligned}$$

Therefore, the increase in the in-band radiation due to the zero order is 28.

Increase in the in-band radiation due to the mirror blank:

$$\begin{aligned} \text{PD4(Be-mirror)/PD4(Be-mono)} &= 26/0.31 = 83.87 \\ \text{PD4(Si-mirror)/PD4(Si-mono)} &= 60/0.76 = 78.94 \\ \text{PD4(empty-mirror)/PD4(empty-mono)} &= 170/1.85 = 91.89 \end{aligned}$$

Therefore, the increase in the in-band radiation due to the mirror blank is 80. It should be emphasized that this data was taken with 300 line/mm grating which has higher resolving power than 200 lines/mm with which the defect counting experiment was performed. Generally it is believed that the efficiency of the 200 lines/mm is 4 times higher than that of 300 lines/mm. In other words, the flux increase from the 200 lines/mm grating to mirror blank is $80/4 = 20$ times, which is in synch with the bandwidth argument.

(4) Calculation of the total number of inband photons after the 25 μm pinhole.

$$\begin{aligned} &\text{PD1(mono-Si)} * (\text{attenuation due to the Si filter}) * (\text{improvement due to the mirror blank}) \\ &= 4 * 2.6 * 80 = 832 \text{ nA} = 832 * 5e8 = 4.16e11 \text{ pps.} \end{aligned}$$

The total incoming inband radiation is 4.16e11 pps after 25 μm pinhole. However, this flux is within the full multilayer inband. When the bandwidth is adjusted due to the bandwidth narrowing from the multiple multilayer mirrors, the available flux is $832 \text{ nA} * 2/3 = 554 \text{ nA}$. Before the pinhole, the flux is $0.513 \text{ uA} * 100 = 51.3 \text{ uA}$. The factor of 100 comes from the assumption that the transmission through 25 μm pinhole is 1 %.

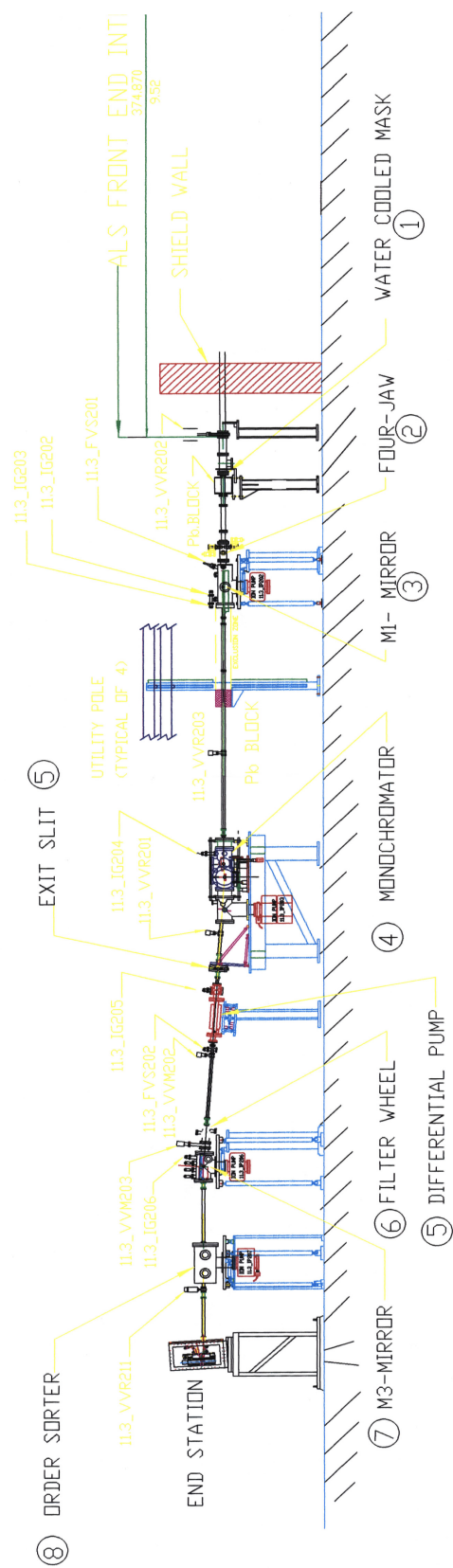
(5) Contribution of the UV into the data.

The contribution of visible or UV that survives after the multilayer bounce can be estimated by comparing PD4(empty-mirror) and PD4(Be-mirror). The Be attenuates the in-band radiation signal by 6.5 times. Therefore, the signal contribution from the in-band radiation in PD4(empty-mirror) =

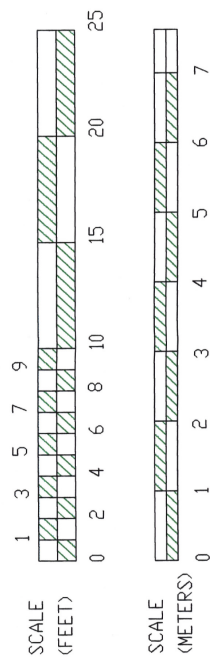
$\text{PD4(Be-mirror)} * 6.5 = 169 \text{ nA}$. This compares fairly good with the measured value of $\text{PD4(empty-mirror)} = 170 \text{ nA}$. Therefore, the contribution of the UV and visible to the photodiode signal is negligible. But the contribution of UV to the dark field signal is something that needs more careful examination

* The throughput of the KB system depends on the overall alignment of the system. When the system is in good alignment, the throughput reaches 30%.

5.2 Side elevation of current beamline



BEAMLINE 11.3.2 ELEVATION VIEW



5.3 Floor plan of beamline

